J. Fluid Mech. (1993), *vol.* 248, *pp.* 315–361
Copyright © 1993 Cambridge University Press

Elliptic jets. Part 3. Dynamics of preferred mode coherent structure

By HYDER S. HUSAIN AND FAZLE HUSSAIN
Mechanical Engineering Department, University of Houston, Houston, TX 77204–4792, USA

(Received 27 April 1992 and in revised form 8 October 1992)

The dynamics of the preferred mode structure in the near field of an elliptic jet have been investigated using hot-wire measurements. A 2:1 aspect ratio jet with an initially turbulent boundary layer and a *constant* momentum thickness all around the nozzle exit perimeter was used for this study. Measurements were made in air at a Reynolds number $Re_{D_e}(\equiv U_e D_e/\nu) = 3.5 \times 10^4$. Controlled longitudinal excitation at the preferred mode frequency ($St_{D_e} \equiv fD_e/U_e = 0.4$) induced periodic formation of structures, allowing phase-locked measurements with a local trigger hot wire. The dynamics of the organized structure are examined from educed fields of coherent vorticity and incoherent turbulence in the major and minor symmetry planes at five successive phases of evolution, and are also compared with corresponding data for a circular jet. Unlike in a circular jet, azimuthally fixed streamwise vortices (ribs) form without the aid of azimuthal forcing. The three-dimensional deformation of elliptic vortical structures and the rib formation mechanism have also been studied through direct numerical simulation. Differential self-induced motions due to non-uniform azimuthal curvature and the azimuthally fixed ribs produce greater mass entrainment in the elliptic jet than in a circular jet. The turbulence production mechanism, entrainment and mixing enhancement, and time-average measures and their modification by excitation are also discussed in terms of coherent structure dynamics and the rib–roll interaction. Various phase-dependent and time-average turbulence measures documented in this paper should serve as target data for validation of numerical simulations and turbulence modelling, and for design and control purposes in technological applications. Further details are given by Husain (1984).

1. Introduction

After having established some of the basic differences between circular and elliptic jets (Hussain & Husain 1989; Husain & Hussain 1991; referred to herein as Part 1 and Part 2 respectively), we discuss in this final part the dynamics of the preferred mode coherent structure in the near field of an elliptic jet. Part 1 addressed the effects of curvature variation of the vortical structures (rolls) which lead to three-dimensional deformation due to non-uniform self-induction, and the effects of initial conditions, aspect ratio, and excitation frequency and amplitude on the elliptic jet instability and its evolution. Instability characteristics of the initial shear layer and the jet column modes were reported for jets with uniform and non-uniform momentum thicknesses along the exit plane perimeter. The dynamics of coherent structure pairing were addressed in Part 2. Because of the switching of the original major and minor axes produced by self-induced structure deformation, pairing was found to be

quite different from that in a circular jet. In this part we discuss the preferred mode structure dynamics in the near field of an elliptic jet (i.e. with pairing suppressed).

In turbulent shear flows, we distinguish coherent structure *modes* by their spatial configuration, such as toroidal, helical, roller, etc. Different flows may be characterized by different modes of coherent structures. Furthermore, even a variety of modes may occur in a particular flow. In a given flow, if a particular mode dominates – both statistically and dynamically – we designate it as the *preferred mode*. The importance of the preferred mode structure lies in the fact that it is the most frequently occurring and dominant of all large-scale coherent structures which occur naturally (i.e. in the absence of excitation.)

A question arises as to whether the preferred mode is particular to axisymmetric jets, or if it is a characteristic feature of all jets, including three-dimensional jets such as square, rectangular, triangular and elliptic. If a preferred mode is generic to all jets, then what are the similarities and differences among the preferred mode structures in these jets? The study of elliptic jets is interesting for two major reasons. First, it is an intermediate configuration between the two simple, and extensively studied, asymptotic geometries: circular and plane jets. Although the existence of two geometrical lengthscales (i.e. major and minor axes) makes the problem more complicated, a detailed study of elliptic jets facilitates a better understanding of the wider class of jets where the curvature of the coherent structure changes around the perimeter. Second, studies have revealed that the rectangular structures become elliptic-like soon after their rollup in rectangular jets (Tsuchiya, Horikoshi & Sato 1984). Thus, a systematic study of elliptic jets is also highly relevant to an understanding of the dynamics of rectangular jets, which have important practical applications.

Determination of the jet preferred mode is rather non-trivial, although it is easier in the near field than in the far field. The preferred mode frequency in the near field of an unexcited jet inferred from the velocity spectra peak may vary considerably depending on the sensor's location as well as phase jitter caused by uncontrolled environmental (including upstream) disturbances. Controlled excitation (one frequency at a time) at a level higher than the environmental disturbances produces more organized structures and aids identification of the near-field preferred mode. Such excitation ensures periodic formation of structures, whose significance can be evaluated in terms of the various dynamical measures associated with their evolution.

Studies of excited circular jets over a limited range of Strouhal number (St_D = 0.15–0.5; here St_D is based on the jet diameter D) by Crow & Champagne (1971) revealed that the centreline total turbulence intensity $u'_c(x)$ was maximally amplified at $St_D = 0.3$; this result led them to conclude that $St_D = 0.3$ was the preferred mode frequency of the jet. By extending the range of excitation, Zaman & Hussain (1980) found that $u'_c(x)$ is maximally amplified at $St_D \approx 0.85$, not at $St_D \approx 0.3$, as a result of subharmonic resonance at this frequency, which produces spatially fixed periodic vortex pairing. Following Crow & Champagne, $St_D \approx 0.85$ would thus have been called the preferred mode. However, Zaman & Hussain (1980) redefined the preferred mode as the frequency that produces the maximally amplified *fundamental* amplitude u'_f (instead of the total turbulence level u'_c) and found that u'_f reached its maximum at $St_D \approx 0.35$, establishing this as the preferred mode. Published literature on excited and unexcited circular jets show a wide variation (St_D = 0.3–0.64) in the preferred mode frequency (see, for example, Gutmark & Ho 1983). However, such a variation in the observed values of the preferred mode frequency is not an indication of the

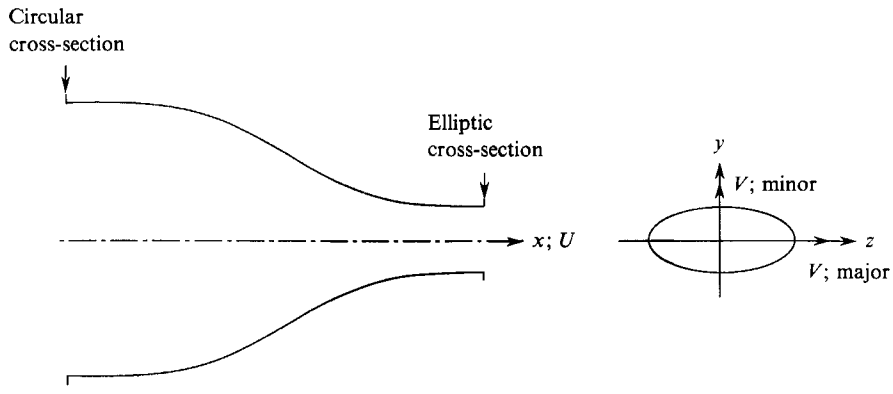

FIGURE 1. Schematic of the elliptic nozzle showing the coordinate system.

lack of universality of either the preferred mode concept or the St_D value, but merely of the fact that its value depends crucially on the method of determination. In order to unambiguously determine the preferred mode frequency in the near field of a jet, not only should the jet be studied under controlled excitation, but the measurement location must also be agreed upon. In reality, no practical jet is unexcited; natural jets are subject to uncontrolled environmental noise and upstream perturbations. Controlled excitation, if of a sufficient level, can overshadow the effects of uncontrolled disturbances, allowing precise determination of the preferred mode frequency. Regarding measurement location, it was observed that the spectral peak frequency not only varies in x (typically decreasing in x due to pairing), but also in the radial direction (as much as threefold) across the mixing layer (Hussain 1983). In this respect, u_f' measurements on the jet axis ($x/D \approx 2$) under single-frequency controlled excitation provides the least ambiguous data.

Controlled excitation paces the initiation of vortical structures, but has very little effect on their evolution downstream. The determination of the preferred mode in the far field of a jet is more difficult than in the near field because variance in structure shape, size, strength, and orientation increases with downstream distance. In this case, preferred mode(s) should be determined from the multidimensional probability density functions (p.d.fs) of the characteristic parameters, e.g. shape, size, orientation, and strength. Peaks in these p.d.f. distributions identify preferred modes with the dominant peak called 'the preferred mode' (e.g. Hussain 1983). Equivalently, preferred modes correspond to dense clusters in a feature space defined by these parameters or to the formation of trajectory bundles of coherent structures in phase space.

The relevance of studies based on excitation-induced structures to the understanding of naturally occurring structures is certainly a valid concern. There are two rather strong reasons which justify the use of controlled excitation in coherent structure studies. First, controlled excitation at the preferred mode frequency induces the most dominant structures to form periodically, and it also standardizes their evolution up to a certain distance from the jet exit plane. Excitation prevents the formation of weak or non-dominant structures that may otherwise be triggered by uncontrolled perturbations. Second, the controlled passage of the structures permits eduction of their details through the much simpler method of phase averaging, which makes use of the excitation period as a phase reference. Hussain & Zaman (1981) argued and demonstrated by experimental data that at small excitation amplitudes, the structure details and evolution induced via preferred

mode excitation were similar to those in unexcited flows. The structure evolution will be different if the excitation is too strong (even at the preferred mode) or if unusual interactions are induced through excitation.

In Part 1 we showed that elliptic jet near-field coherent structures, like those of axisymmetric jets, are characterized by the 'preferred mode' which scales with the *equivalent diameter* $D_e = 2\,(ab)^{\frac{1}{2}}$ (where a and b are the semi-axis) of the elliptic nozzle exit (see also Husain & Hussain 1983). The corresponding Strouhal number ($St_{D_e} \equiv fD_e/U_e$) based on D_e was found to be approximately 0.4, irrespective of whether the exit plane boundary layer was laminar or turbulent.

Once again, we investigate here the dynamics of the preferred mode coherent structure in the near field of a moderate-aspect ratio elliptic jet under controlled excitation by phase-locked measurement and numerical simulation. From these data we examine structure properties, such as coherent velocity and vorticity, incoherent turbulence intensity, coherent and incoherent Reynolds stress, and turbulence production.

The organization of the material in this paper is as follows. In §2, we discuss experimental procedures which also include documentation of initial conditions (§2.1), jet response to excitation (§2.2), data acquisition procedure (§2.3) and the numerical technique (§2.4). Section 3.1 addresses coherent vorticity distribution, vortex trajectories and vorticity diffusion in the major and minor planes, and compares these with those in the circular jet. Direct numerical simulation is used to discuss the development of roll three-dimensionality, and the formation of ribs; and the interaction of these structures are discussed in §3.2. In §3.3, other coherent structure properties (e.g. coherent velocities, incoherent turbulence intensities, coherent and incoherent Reynolds stresses), mass entrainment and turbulence production mechanism are discussed. Finally, time-average properties with and without the preferred mode excitation are discussed in §3.4. Concluding remarks are given in §4. Further details of apparatus, procedures and data are documented in Husain (1984).

2. Experimental procedure

The experiments were carried out in a variable-speed jet facility, in which nozzles of different sizes and shapes can be utilized. Details of the jet facility are described in Part 1. Figure 1 depicts the coordinate system used in this study. Because the elliptic jet cross-section switches axes, reference planes need to be clearly specified. We use 'major plane' and 'minor plane' to denote the reference planes containing the jet axis and the major and minor axes, respectively, at the nozzle exit. In addition, we frequently refer to the structure's segments which intersect these planes as the 'major-axis side' and 'minor-axis side'.

For the present study we used a 2:1 aspect ratio elliptic nozzle ($D_e = 5.08$ cm) with a turbulent boundary layer of *constant momentum thickness* θ_e all around the nozzle exit perimeter (nozzle N4 described in Part 1). The importance of a constant θ_e was explained in Part 1, which also emphasized the role of the initial condition (i.e. exit flow details) in the evolution of free shear flows.

2.1. *Initial conditions*

For the data in the present paper, the exit speed was held fixed at 10 m s^{-1} which corresponded to a jet Reynolds number $Re_{D_e} = 3.5 \times 10^4$. In general, θ_e of a contoured elliptic nozzle varies significantly along the exit perimeter because the wall

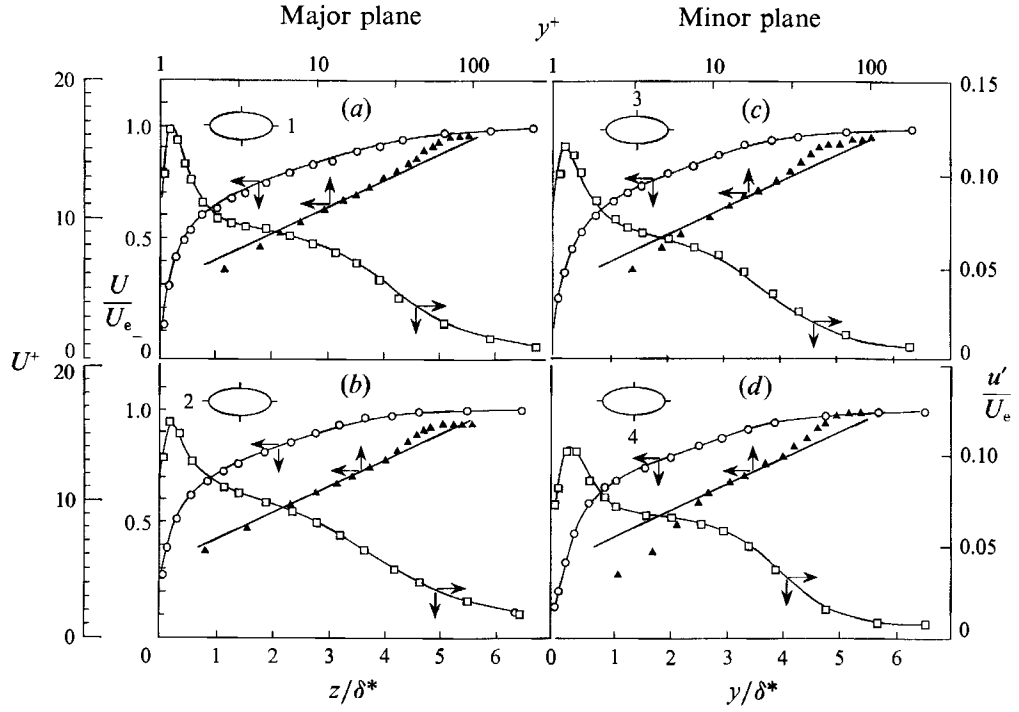

FIGURE 2(*a–d*). Boundary-layer characteristics at four locations in the exit plane. Measurement locations are shown by numbers at the upper left-hand corner in each figure. ○, U/U_e; □, u'/U_e; ▲, U^+. Note that the y^+-axis relates to U^+ data only. Solid line represents $U^+ = 5.6\log_{10} y^+ + 4.9$.

lengths and curvatures are different in the major and minor planes due to the change from a circular to an elliptic cross-section. A turbulent boundary layer with a nearly constant θ_e was achieved by attaching a sandpaper trip ring of varying width 4 cm upstream of the nozzle exit. The exit boundary layer was measured in both major and minor planes to check its uniformity and quality. The variation in θ_e was within 1.5% of the mean value (0.71 mm) at these locations. Figure 2(*a–d*) shows the profiles of the exit boundary-layer mean velocity (both U/U_e *vs.* y/δ^* and U^+ *vs.* y^+) and longitudinal fluctuation intensity (u'/U_e *vs.* y/δ^*). The boundary layer was inferred to be fully developed turbulent based on these profiles and have a broadband, smooth u-spectra (not included in figure 2). The mean velocity profile had a shape factor of 1.4, and was found to consist of distinct logarithmic and wake regions in the universal (U^+, y^+) coordinates (see Part 1 for details). All of these measures are consistent with flat-plate turbulent boundary layers at the same $U_e\theta_e/\nu$. For comparison, the universal relation for flat-plate boundary layers (Coles 1962), namely, $U^+ = 5.6\log_{10} y^+ + 4.9$, is shown as a solid line. Note that the azimuthal homogeneity of the exit boundary layer is apparent from the uniformity of the U and u' profiles at these locations.

2.2. *Response to excitation*

In order to obtain phase-locked measurements, periodic structure formation was induced using excitation at the preferred mode frequency (i.e. at $St_{D_e} = 0.4$) with an exit excitation amplitude of $u'_e/U_e = 2.5\%$. Controlled longitudinal plane-wave excitations were introduced at the jet exit via resonance of the settling chamber cavity (see figure 1*a* of Part 1). A loudspeaker attached to the first settling chamber

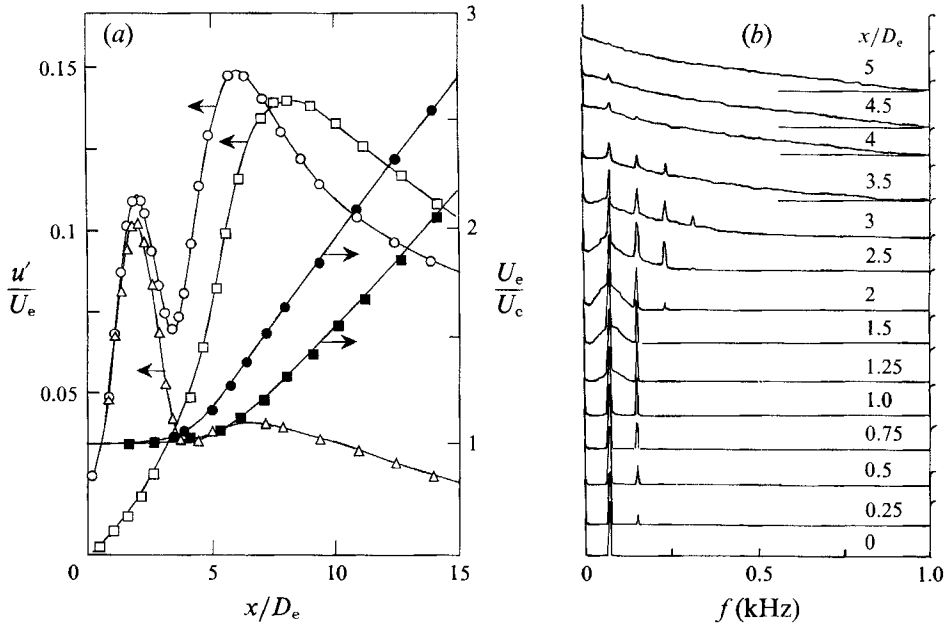

FIGURE 3. (*a*) Response of the jet under excitation at the preferred mode frequency $St_{D_e} = 0.4$; □, u'_c unexcited; ○, u'_t excited; △, u'_f excited; ■, U_c unexcited; ●, U_c excited. (*b*) Evolution of u-spectrum along the jet centreline under excitation at $St_{D_e} = 0.4$; ordinate scale is logarithmic (arbitrary).

was driven by a sinusoidal signal from an oscillator to induce the cavity resonance. The exit-plane velocity perturbation was sinusoidal with negligible harmonic content.

Since the present experiments were performed at a much lower value of Re_{D_e} (3.5×10^4) than that of Part 1 ($Re_{D_e} = 10^5$), the preferred mode frequency was checked at this Re_{D_e} and again found to occur at $St_{D_e} = 0.4$. This is consistent with our claim that the preferred mode is fairly independent of Re_{D_e}, at least within this Re_{D_e} range. Experiments at a lower Re_{D_e} produce better spatial resolution because the structures are larger at lower speeds.

Centreline time-average measures U_c/U_e, u'_c/U_e and u'_t/U_e for excited ($St_{D_e} = 0.4$) and unexcited jets are shown in figure 3(*a*). Here, U_c and u'_c are the mean and total r.m.s. fluctuation values of the streamwise velocity, and u'_t is the corresponding r.m.s. amplitude of the fundamental. Excitation produces a peak in the $u'_c(x)$ distribution at $x/D_e \approx 2$ with the predominant contribution to this peak from u'_t. Note that for the excited case, the distribution of $u'_t(x)$ nearly coincides with that of $u'_c(x)$ up to $x/D_e \approx 2.5$. This peak in $u'_c(x)$ at $x/D_e \approx 2$ is evidently the 'footprint' of the rollup of preferred mode structures at this location.

Figure 3(*b*) shows the centreline evolution of the u-spectrum in log-linear coordinates. The spectra, averaged over 128 realizations, were obtained with a real-time spectrum analyzer (Spectroscope SD335). The spectral peak at the fundamental frequency (i.e. at the driving frequency $f = 80$ Hz) grows to its maximum at $x/D_e \approx 2$, then decays until it finally becomes submerged in the evolving turbulence at $x/D_e \approx 5$; beyond this location, the spectrum is fully developed and free from any noticeable peak. However, this does not mean that turbulence is fine-grained beyond $x/D_e \approx 5$. At this location, the preferred mode structures are in a state of large-scale

breakdown and have lost their phase coherence so that the random phase leaves no discernible spectral peak. The absence of any subharmonic peak in the spectrum at any x-location confirms that under preferred mode excitation, the structures evolve without any pairing, which is also consistent with the preferred mode behaviour in circular jets (Hussain & Zaman 1981).

2.3. *Data acquisition*

The advantages and limitations of various coherent structure eduction methods have been discussed in Part 2. Phase-locked measurements were carried out under controlled excitation, employing signals from a reference trigger probe (single wire) in the flow field to detect the phase of the advecting structures. Eduction involves the decomposition of any field quantity $g(x,t)$ into coherent $\langle g \rangle$ and incoherent g_r components through phase averaging at a particular phase (Hussain 1983).

In the present case, the trigger probe was placed on the jet centreline at a location X_M where the educed structure was expected to be centred. The reference signal was bandpass filtered to remove the d.c. and high-frequency oscillations before being passed to the triggering device. The details of the triggering and data acquisition techniques were discussed by Hussain & Zaman (1980). Data were computer-sampled from the measuring probe (X-wire) at the instant when the triggering device indicated peaks in the periodic $u(t)$ signal. For a given location of the X-wire, an average over a large ensemble (typically 2000–3000 samples, which gave convergence of $\langle u \rangle$ and $\langle v \rangle$ within 5%) of data obtained at successive trigger times produced the phase-average measures. Note that the phase of the reference signal was chosen so that the phase-average longitudinal velocity $\langle u(x) \rangle$ was expected to have a peak at $X \approx X_M$ on the jet centreline. With the trigger setting unaltered, the measuring X-probe scanned the measurement region to obtain on-line data and compute various structure characteristics, namely streamwise and transverse phase-average velocities ($\langle u \rangle$, $\langle v \rangle$), azimuthal coherent vorticity ($\langle \omega \rangle$), incoherent turbulence intensities ($\langle u_r \rangle^{\frac{1}{2}}$, $\langle v_r \rangle^{\frac{1}{2}}$), coherent and incoherent Reynolds stresses ($\langle u_p v_p \rangle$, $\langle u_r v_r \rangle$), and coherent turbulence production ($\langle P \rangle$). These quantities were measured in five successive downstream regions in both the major and minor planes with the reference probe located correspondingly at $x/D_e = 1$, 1.75, 2.25, 3 and 3.5. Coherent structure measures at these locations represent five successive phases (denoted phases I–V) of the preferred mode structure evolution.

For comparison, the preferred mode coherent structures in a circular jet were also educed under the same conditions (i.e. same nozzle exit area, exit velocity, turbulent exit boundary layer, excitation level and Strouhal number, using the same instrumentation and facility, but with a circular nozzle). Due care was taken to check the exit turbulent boundary-layer characteristics (mean and fluctuation level profiles) and their axisymmetry.

2.4. *Numerical simulation*

Since the hot-wire measurements were limited to only two planes (i.e. the major and minor planes) and the technique used here cannot measure streamwise vorticity, we used direct numerical simulation (code developed by M. V. Melander; see Melander, Hussain & Basu 1991) to examine the spatial details of the structures' evolution and interaction. The incompressible Navier–Stokes equations were integrated in a 64^3 periodic box using spectral methods. The calculations were fully dealiased with 2/3 k-space truncation, and a fourth-order predictor-corrector time-stepping scheme was used.

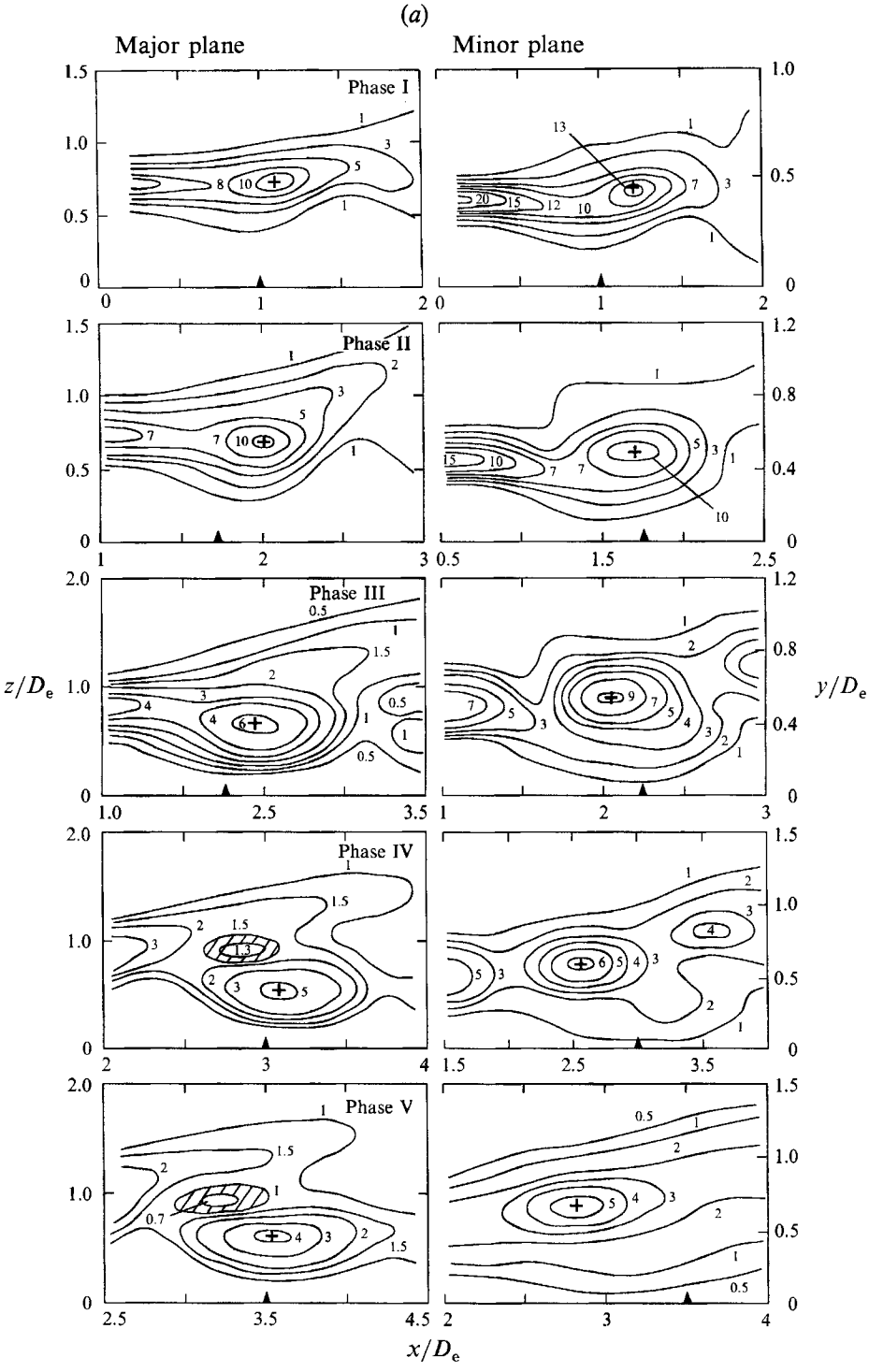

FIGURE 4(a). For caption see facing page.

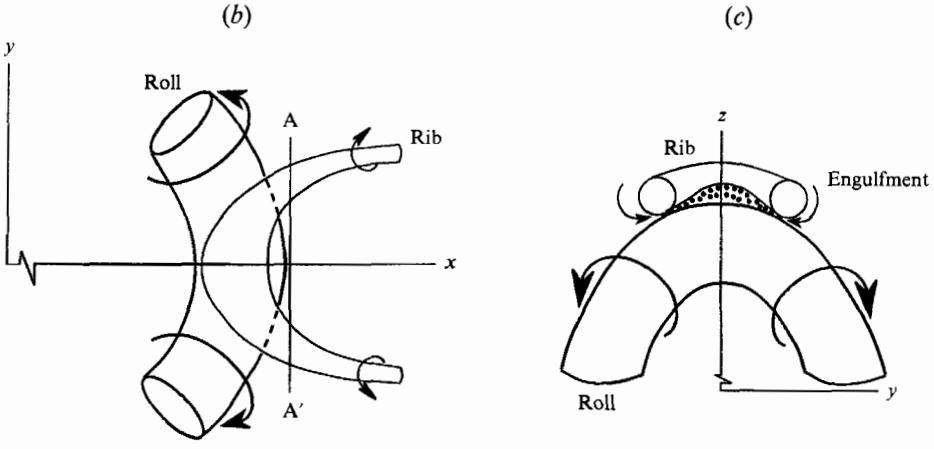

FIGURE 4. (*a*) Contours of coherent azimuthal vorticity $\langle\omega\rangle/f$ at successive phases (I–V) during preferred mode structure evolution in the elliptic jet. (*b*, *c*) Schematics showing how rib–roll interaction engulfs ambient fluid: (*c*) is a view of (*b*) through section A–A′ looking from the right-hand side.

The flow initialization consists of a top-hat velocity profile with an elliptic base and a constant initial momentum thickness. In addition, a streamwise perturbation of the form $u(x,0) = A\sin(2\pi x/\lambda)$ is added at $t = 0$; here A and λ are the amplitude and perturbation wavelength. For the simulation, the Reynolds number $Re_{D_e} = U_e D_e/\nu$ was 1500, A was 5%, and St_{D_e} is defined in terms of λ as $St_{D_e} \equiv fD_e/U_e = (U_e/2\lambda)(D_e/U_e)$. In the present case, $U_e = 1$, $\lambda = 32$ grid lengths, $a = 18$ grid lengths and $b = 9$ grid lengths give $St_{D_e} \approx 0.4$, the jet column preferred mode frequency. The definition of 'preferred mode' and the reason for selection of this value were discussed in Part 1. Non-dimensional time t^* is defined as tU_e/D_e.

Unlike a circular vortex ring, an elliptic vortex ring possesses the intrinsic azimuthal instability mode 2 and its higher harmonics (Bridges & Hussain 1988). Thus, in an elliptic jet simulation, no azimuthal perturbation is necessary to initiate the formation of streamwise vortices, which are induced inherently by mode 2.

There are subtle differences between temporally and spatially evolving jets (Corcos & Sherman 1984). However, the instantaneous small-scale as well as local dynamics involving the deformation of elliptic structures, the formation of longitudinal vortices, and mixing (ejection of jet core fluid and ingestion of ambient fluid) can be studied in detail through temporal simulation, which permits higher resolution and is computationally far less demanding than the corresponding spatial simulation. Consequently, a temporally evolving elliptic jet was simulated to aid interpretation of the laboratory data.

3. Results and discussion

The spatial distributions of various phase-average measures are presented as contour plots. Positive-valued contours are denoted by solid lines and negative-valued ones by dashed lines. In each figure, a triangle on the abscissa identifies the location of the trigger probe, and the centre of the coherent structure (i.e. the location of the peak azimuthal vorticity) is marked +.

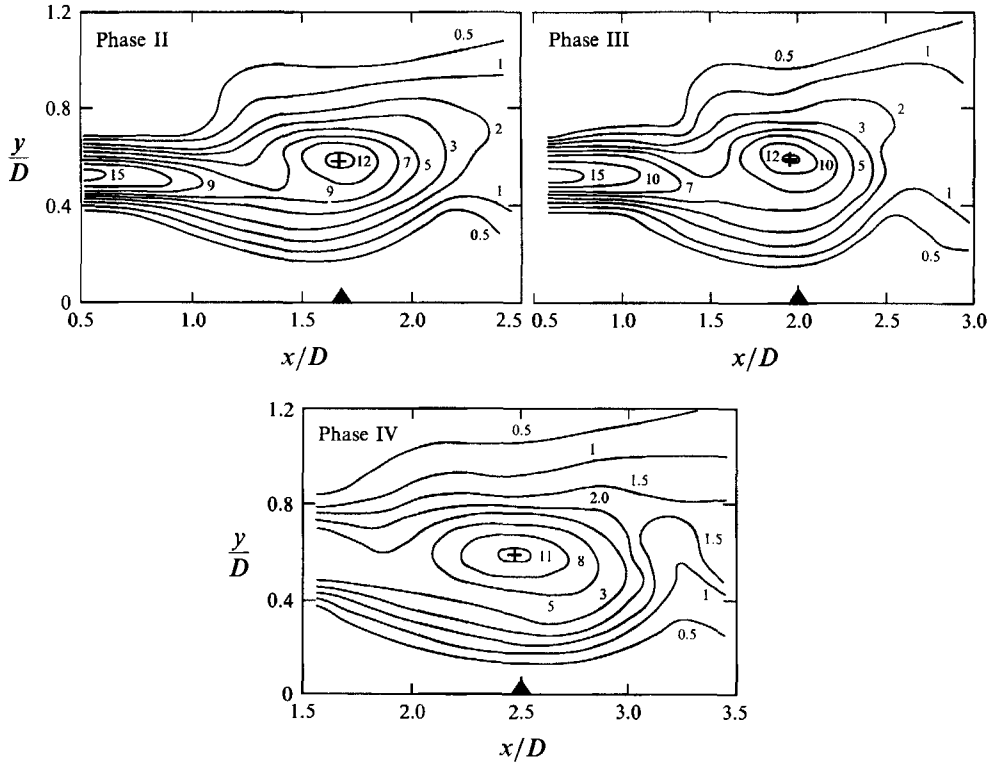

FIGURE 5. Contours of coherent azimuthal vorticity $\langle\omega\rangle/f$ at successive phases (II–IV) during preferred mode structure evolution in the circular jet.

3.1. *Coherent vorticity*

The distribution of experimentally obtained coherent azimuthal vorticity $\langle\omega\rangle$, non-dimensionalized by the excitation frequency f, is shown in figure 4(*a*) for five sequential phases (I–V) of the preferred mode structure evolution in both the major and minor planes. Structures in the circular jet were educed at three phases, corresponding approximately to phases II, III and IV of the elliptic structure evolution in the minor plane. Contours of $\langle\omega\rangle/f$ for the circular jet are shown in figure 5.

3.1.1. *Vorticity distribution*

Since the elliptic jet preferred mode structures undergo continuous deformation due to curvature-dependent self-induction, one expects that the details of the coherent structure evolution (i.e. orientation, peak vorticity, vorticity diffusion and vortex stretching) in the two planes will be different and also different from circular jet data.

Unlike in the minor plane or in the circular jet, the low-level contours (e.g. $\langle\omega\rangle/f = 1, 1.5$) form an S-shaped fold in the major plane at phase III. At a later phase, (e.g. phase IV) a region of reduced vorticity (i.e. a valley) is developed upstream of the fold, as shown hatched in figure 4(*a*). The mechanisms that seem responsible for the formation of the fold and valley are as follows. As the vortex core in the major plane advects toward the jet axis by self-induction, it leaves behind low-vorticity fluid which forms the fold. Note that at phase I, the closed vorticity contours (e.g.

$\langle\omega\rangle/f = 8$, 10 in the major plane and $\langle\omega\rangle/f = 12$, 13 in the minor plane) indicate vortex sheet rollup due to the Kelvin–Helmholtz instability. However, unlike in the minor plane, the low level contour $\langle\omega\rangle/f = 3$ at phase I in the major plane remains elongated in the streamwise direction; the downstream tip of this contour is displaced substantially from the vorticity peak. This suggests that the rollup is less complete in the major plane. As the vortex core in the major plane advects toward the jet axis, the low-vorticity fluid on the zero-speed side does not follow the motion of the vortex core. Such differential motion of the vortical structure produces the observed S-shaped kink of the low-level vorticity contours.

The interaction of the roll with streamwise vortices (ribs) engulfs ambient fluid between the roll and the rib to form the valley. (The rib formation mechanism and rib–roll interaction are discussed in detail in §3.2.) In figure 4(*b*, *c*), we show schematically how the rib–roll interaction engulfs ambient fluid. Figure 4(*b*) shows the major-axis side of the roll (top view) where the rib vortex is advected over the roll onto the zero-speed side, and figure 4(*c*) is a view through section A–A′. The rotational motion of the ribs pumps ambient fluid from the zero-speed side, while rolls pump core fluid into the space between the roll and the flattened rib. Simultaneously, vorticity from the rib and roll is diffused to this fluid, which produces the closed low-level contours in this region (forming the valley).

Contour patterns in the minor plane are qualitatively similar to those in the circular jet, especially at earlier phases. However, at later phases subtle differences develop. Vorticity contours in the circular jet remain fairly symmetric about the vortex centre, while the contours in the minor plane exhibit asymmetry. Also, the low-vorticity contours in the minor plane, e.g. $\langle\omega\rangle/f = 0.5$, 1 are much closer to the jet axis. In this plane, the rib approaches the roll from the high-speed side and the self-induction pushes the rib's tip toward the jet axis, resulting in larger $\langle\omega\rangle$ near the jet axis (see §3.2).

The second peak vorticity region (near the top right-hand corner) at phase IV of the minor plane is the remnant of the previous (i.e. downstream) structure, which is presumably on the verge of breakdown and is not captured at phase V.

3.1.2 *Vortex trajectories*

The three-dimensional deformation of the elliptic structure is evident from the relative x, y and x, z locations of vortex centres in the two planes (figure 4). At phase I, the vortex centres in both planes lie at nearly the same x. That is, the elliptic vortex at this phase is nearly planar and parallel to the exit plane. However, as the structure evolves (phases II–V), the major-axis side moves ahead of the minor-axis side and toward the jet axis because of differential self-induction due to greater curvature of the former. The forward inclination of the major-axis side in turn produces curvature on the minor-axis side, resulting in self-induced motion directed away from the jet axis. As a result, the vortex core in the minor plane gradually moves away from the jet centreline.

The trajectories of the preferred mode structure in the two planes are shown in figure 6. (In figures 6–8 and 17 D denotes both circular jet diameter and elliptic jet equivalent diameter D_e.) In this context, 'trajectory' refers to the path of the vortex core centre, specified as the location of peak coherent vorticity. For comparison, vortex trajectories of the circular jet (present study and from Hussain & Zaman 1981) are also included. The two independent data sets for the circular jet show a small difference in the vortex trajectories during the first two phases, presumably due to the difference in the initial excitation levels used. The excitation level was

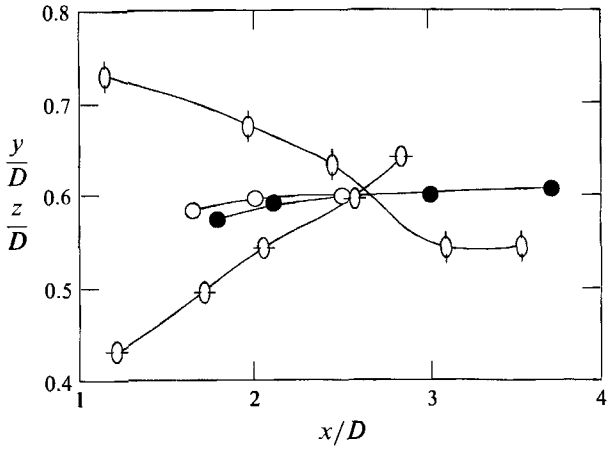

FIGURE 6. Vortex trajectories of the preferred mode structure in circular and elliptic jets. ⊖, major plane; ⊖, minor plane; ○, circular jet (present); ●, circular jet (Hussain & Zaman 1981).

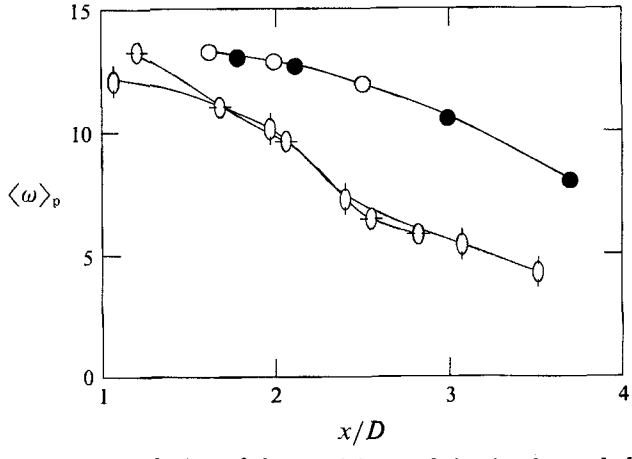

FIGURE 7. Downstream evolution of the vorticity peak in circular and elliptic jets. Symbols are the same as in figure 6.

2.5% in the present experiment, but 2.0% in that of Hussain & Zaman. A higher level of excitation should cause the structure to roll up closer to the exit plane and to achieve its asymptotic diameter earlier.

As shown in figure 6, unlike in a circular jet, the vortex cores in the major and minor planes move respectively toward and away from the jet axis. The inward motion of the roll in the major plane brings ambient fluid with it toward the jet axis, while the outward motion in the minor plane transports jet core fluid and ejects it farther into the ambient. The advection of such deforming elliptic structures may provide better mixing in an elliptic jet than in a circular jet. Note that the crossing of the vortex trajectories in the major and minor planes at $x/D_e \approx 2.6$ indicates the switching of axes. Unlike an isolated elliptic vortex ring, the switching of axes of vortical structures in an elliptic jet does not continue indefinitely (Part 1). In the present case, the original preferred mode structure breaks down shortly after the first switching near the end of the potential core. Thus the structures could not be educed for $x/D_e > 4$ using the present technique.

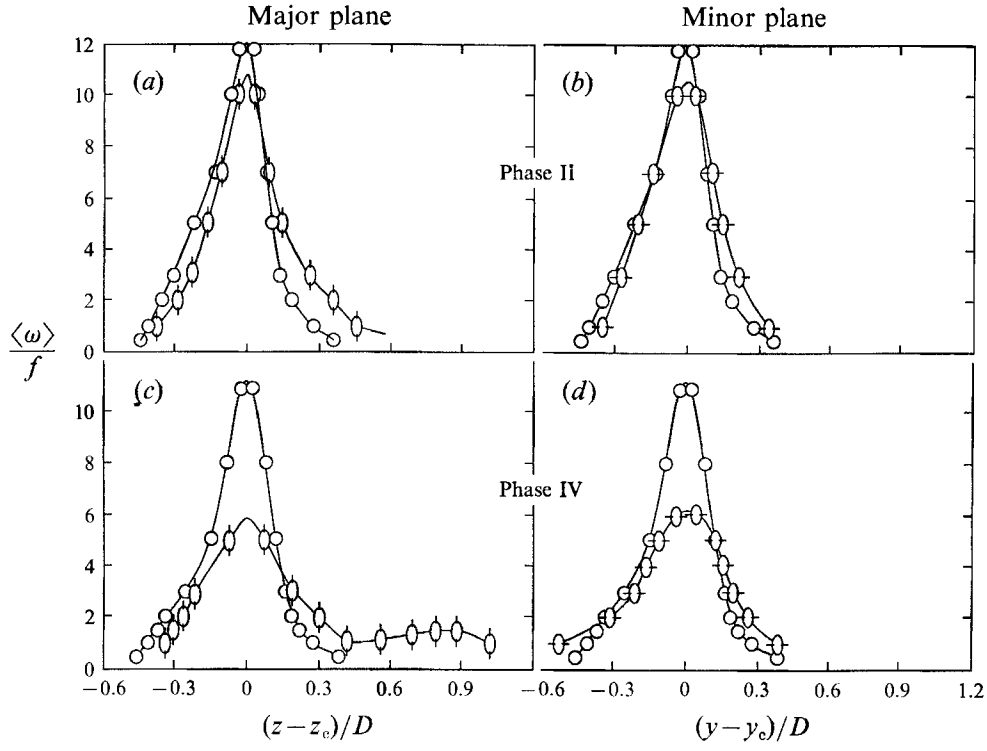

FIGURE 8. (*a–d*). Radial profiles of $\langle\omega\rangle/f$ through the vorticity peak location in circular and elliptic jets for phases II and IV. Symbols are the same as in figure 6.

3.1.3. *Peak vorticity and vorticity diffusion*

The decay of the coherent vorticity peak $\langle\omega\rangle_p$ during the evolution of the preferred mode structure is shown in figure 7 for both elliptic and circular jets; $\langle\omega\rangle_p$ decays faster in the elliptic jet up to $x/D_e \approx 2.5$. The peak value of incoherent turbulence intensity is found to be higher (by 10–20%) in the elliptic jet, which presumably causes faster diffusion of the peak vorticity in the elliptic jet.

A comparison of $\langle\omega\rangle$ contours in the circular and elliptic jet shows that $\langle\omega\rangle$ is more diffuse at later phases in the latter. This is highlighted by the radial profiles of $\langle\omega\rangle/f$ through the vortex centre shown in figure 8(*a–d*) for phases II and IV. In these figures, the origin of the transverse coordinate is shifted to the location of the vortex centre (by an amount y_c in the minor plane and z_c in the major plane). In the circular jet, the $\langle\omega\rangle$ profiles show no significant differences between phases II and IV, indicating that very little vorticity has been diffused. At phase II, $\langle\omega\rangle$ profiles in both planes of the elliptic jet are qualitatively similar to those in the circular jet, although there is more spreading on the zero-speed side in the major plane. At phase IV, the decrease in the peak vorticity is quite significant in the elliptic jet. In addition, the spreading of low-level vorticity in the major plane is enhanced by fold formation. Analysis of flow visualization pictures, and vortex centre locations in the two planes of the elliptic jet show that the vortex circumference has increased by roughly 10% between phase I and IV due to stretching caused by differential advection of the major- and minor-axis sides. However, the faster decay of $\langle\omega\rangle_p$ and spreading of the $\langle\omega\rangle$ profile suggest that the diffusion of vorticity by incoherent turbulence dominates the enhancement by stretching.

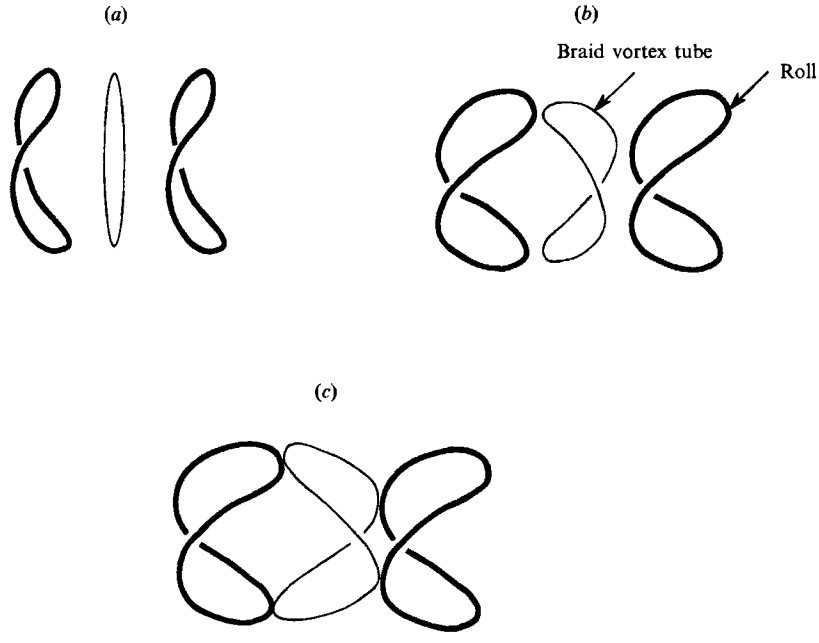

FIGURE 9. (*a–c*). Schematics showing the formation of ribs in the elliptic jet.

3.2. *Three-dimensional development*

3.2.1. *Development of roll three-dimensionality and rib formation*

Having discussed the experimental preferred mode structure in the two symmetry planes, we now discuss the three-dimensional details, such as the deformation of the elliptic jet preferred mode structure, the formation of ribs, and the interaction of these structures based on simulation data. Martin & Meiburg (1991) simulated an axisymmetric jet by means of vortex filaments (which ignores core dynamics) and explained the generation of streamwise vorticity in terms of two induced motions: (*a*) 'global induction' (which we suggest be called *advection*) that pushes downstream those segments of the filament that are closer to the jet axis ahead of those that are away from the jet axis; and (*b*) local induction (i.e. self-induction) which tends to advect the outer sections of the filament of a greater curvature at a faster rate. In the circular jet simulation with small radial perturbations, Martin & Meiburg found that, not surprisingly, advection dominates self-induction in rib formation. In the elliptic jet, a top-hat exit velocity profile (with an elliptic base) initially produces no roll deformation by advection; curvature-dependent self-induction is the dominant mechanism that initiates three-dimensionality of the rolls. In this section we first propose a qualitative description of the rib generation mechanism and then present results from numerical simulation as support.

As discussed earlier, immediately after roll formation, the major-axis sides move ahead because of self-induction. (Self-induced velocity $\boldsymbol{u}_s = \boldsymbol{b}_n(\Gamma/4\pi\rho)\ln(\rho/\sigma)$, where Γ is circulation, ρ radius of curvature, σ core radius and $\boldsymbol{b}_n$ the binormal; for details, see Arms & Hama 1965, Batchelor 1967.) During the rollup process, the region between two neighbouring rolls – the saddle or braid – becomes depleted of vorticity because of migration along the diverging separatrix into the roll. One can model the thin vorticity layer in the braid as a collection of infinitesimally thin vortex tubes of

low strength. It is reasonable to assume that vortex lines are approximately material lines in the braid, at least for short times, and that the deformation of these tubes can be studied by inviscid advection and induction effects on vortex lines.

In contrast to the rolls, the braid vortex tubes experience very little self-induced deformation due to their relatively low circulation. As a result, they should remain nearly planar until the stronger upstream and downstream rolls become substantially deformed. However, the elliptic vortex tubes in the braid eventually deform due to differential induction of the distorted neighbouring rolls. A sequence of the deformation of a typical vortex tube in the braid by this effect is shown schematically in figure 9(*a–c*). Note that the advection of a central vortex tube by the upstream and downstream rolls is imbalanced because of unequal distances between the tube and neighbouring rolls. The induction by the major-axis side of the upstream roll pulls the corresponding side of a braid vortex tube upstream, while the minor-axis side of the downstream roll pulls the tube's minor-axis side downstream. Thus the vortex tubes in the braid become deformed and progressively aligned in the streamwise direction, and their major- and minor-axis sides approach the upstream and downstream rolls, respectively, as depicted in figure 9(*c*).

Vortex lines. From the numerical simulation, vortex lines passing through the rolls and the braid are shown in figure 10(*a–i*) for $t^* = 2.4$, 3.2 and 4.4. At each t^*, three views (projections on the minor and major planes, and a front view) are shown. In these figures, constant-vorticity-level surfaces (50% of the instantaneous peak value $|\omega|_p$) are also superimposed on one symmetric half of the flow to show the relative positions of the vorticity surface and vortex lines. To aid in visualization, simplified perspective views of the rib and roll vortex lines are shown schematically in figure 10(*j–l*). Of the three vortex lines shown in the braid region (figure 10*j*), only the middle vortex line is shown in figure 10(*k*, *l*) to emphasize its deformation by the roll's induction. As expected, the vortex lines associated with the elliptic rolls show deformation similar to that of the structure, while the vortex lines in the braid initially show very little deformation (up to $t^* \sim 2.4$). With increasing time, the major-axis sides of the braid vortex lines are pulled by the upstream roll, while the minor-axis sides are pulled by the downstream roll. This interaction causes the braid vortex lines which were initially in a sheet to cluster and become tilted toward the streamwise direction, illustrating the genesis of streamwise rib vortices (e.g. figure 10*b*, *c*). Note that the tips of the vortex line loops (marked r, s, t in figure 10*f*) are curved outward near the major-axis side of the roll. As the rib vortex lines are pulled toward the major-axis side of the roll by mutual induction, their continual stretching causes further curvature increase. As a result, instead of wrapping around the roll (as might be expected of adjacent like-signed parallel vortex lines), these tips (i.e. r, s, t) of the vortex lines bend radially outward (i.e. toward the zero-speed side) due to this augmentation of self-induction.

On the minor-axis side, the vortex lines are initially pulled toward the jet axis by the downstream roll's induction. Consequently, these vortex lines experience additional stretching due to advection by the core fluid; this in turn increases the curvature and thus self-induction of the pulled-out tips o′, p′, q′ (figure 10*b*), causing them to bend further toward the jet axis. At a later time, when the pulled-out tips advect inside the downstream roll, its induction pulls the tips o, p (figure 10*c*) radially outward. These tips are thus not aligned in the streamwise direction as in the major plane; they are staggered more in the radial direction (as revealed clearly by the vortex lines through the tips o, p, q); the vortex lines through o, p, q are redrawn separately in the insert in figure 10(*c*) for clarity. The front views shown in figure

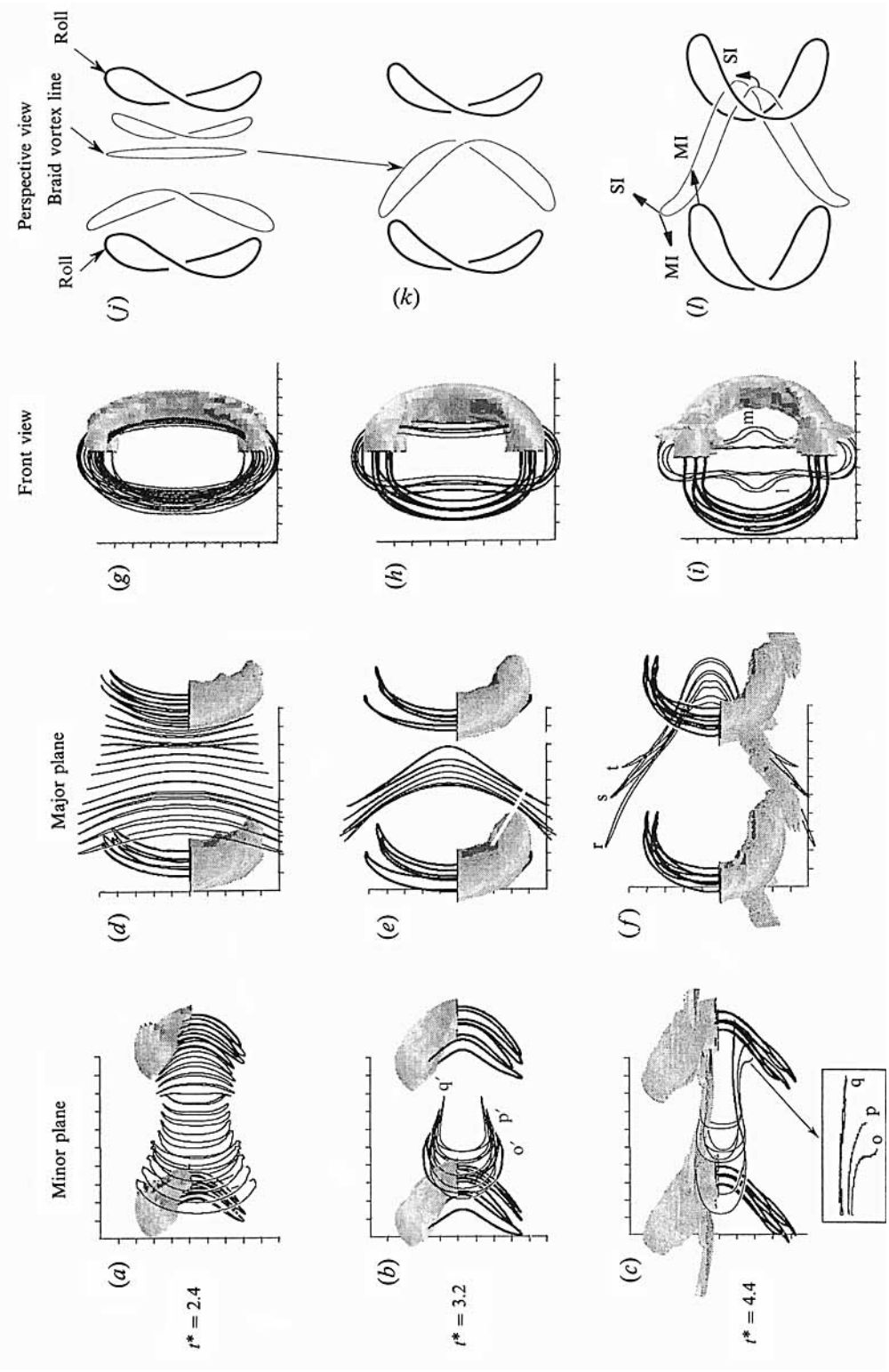

FIGURE 10. Three views of the computed vortex lines at $t^* = 2.4$, 3.2 and 4.4: (*a–c*) minor plane; (*d–f*) major plane; (*g–i*) front view; (*j–l*) schematic of the perspective view. In *l* arrows marked MI and SI indicate the directions of mutual- and self-induced motions respectively.

10(*g–i*) exhibit clearly the radial displacement of the braid vortex lines. The minor-axis sides of the braid vortex lines are first pushed toward the jet axis (figure 10*h*); later at $t^* = 4.4$, the vortex lines closer to the roll (say points l, m in figure 10*i*) are pulled outward. This staggering of vortex line tips in the minor plane produces higher $\langle\omega\rangle$ near the jet axis than in a circular jet as stated in §3.1.1.

Vorticity surface. Having discussed the development of three-dimensionality and the formation of ribs in terms of vortex lines, we now illustrate the evolution of the preferred mode structure and ribs using isosurface plots of instantaneous vorticity magnitude $|\omega|$ at 50% of $|\omega|_p$ for times $t^* = 2.4$, 3.2, 3.6 and 4.4 (figure 11). At each t^*, five views are shown: (*a*) $|\omega|$ surface view showing projection on the minor (x, y)-plane; (*b*, *c*) vorticity contours in the major and minor planes; (*d*) $|\omega|$ surface view projected on the major (x, z)-plane; and (*e*) isometric $|\omega|$ surface. (Note that the staggered rib surface levels in the figures (say at $t^* = 3.2$, 3.6) are artifacts of grid spacing in the numerical simulation.) For $t^* > 4.8$, the structures approach both transverse boundaries of the computational domain, making the simulation unrealistic since the effects of structures in the neighbouring boxes cease to be negligible.

These figures show the gradual bending of the elliptic jet preferred mode structure in the major plane and also show rib evolution. At $t^* = 2.4$, no streamwise vortex is noticeable even at lower levels of $|\omega|$ (not shown). At $t^* = 3.2$, the 50% $|\omega|$ level shows the presence of ribs, but only near the downstream of each major-axis side where vortex stretching is evidently the strongest. A lower level of $|\omega|$ surface shows the ribs extending to both upstream and downstream rolls. At later times ($t^* = 3.6$ and 4.4), the 50% $|\omega|$ surface shows joining of ribs and rolls.

Note that, unlike the measured phase-average vorticity data (figure 4*a*), the instantaneous numerical data shows an increase in the vorticity peak in the major plane (figure 11*b*). This is presumably due to the difference in the initial condition; the initially turbulent boundary layer in the laboratory experiment causes the peak vorticity to decay faster due to a higher level of incoherent turbulence. Also, note that the advection of the vortex core in the major plane (figure 11*b*) toward the jet axis produces an elongated tail in the low-vorticity contours which appears on the major-axis side of vorticity surface plot shown in figure 11(*a*) at $t^* = 3.6$ and 4.4.

Non-uniformities of the roll cross-section are clear from these figures, especially from the vorticity contours in figure 11(*b*, *c*). This is not unexpected because azimuthally non-uniform deformation and stretching lead to four equal roll quadrants, each of continuously varying core cross-section. Melander & Hussain (1992) have shown that an axisymmetric vortex tube with a non-uniform cross-section exhibits strong core dynamics consisting of vorticity wavepackets which travel along the tube axis and induce a strong meridional flow which significantly affects the vortex evolution. This suggests that circular and elliptic vortical structures may evolve quite differently not only because of non-uniform curvature-dependent self-induction but also because of vortex cross-section non-uniformity in the elliptic structure. Thus, a quantitative study of the role of core dynamics in elliptic coherent structures would be informative.

Since the joining of the ribs with the rolls is not clear in these vorticity surface plots, we elucidate our perception of this in figure 11(*f*) for time $t^* \approx 4.4$. This schematic is inferred by observing the structure evolution and interaction (i.e. by observing various levels of vorticity surface, vortex cross-sections and vortex lines) from various view angles of the numerical data using a colour graphic station. The upstream side of a rib joins a roll from the zero-speed side, while the downstream side

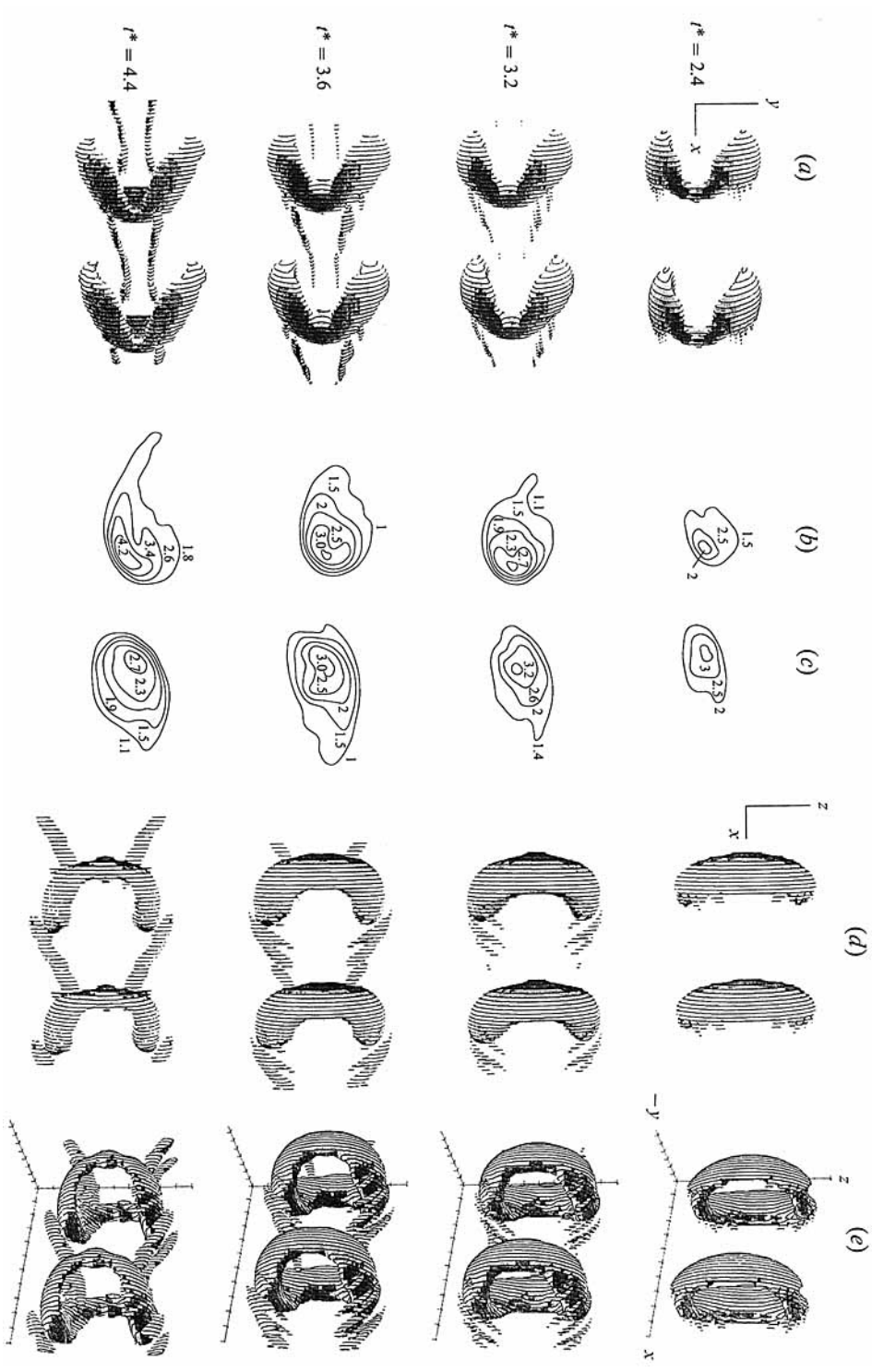

FIGURE 11(*a–e*). For caption see facing page.

(*f*)

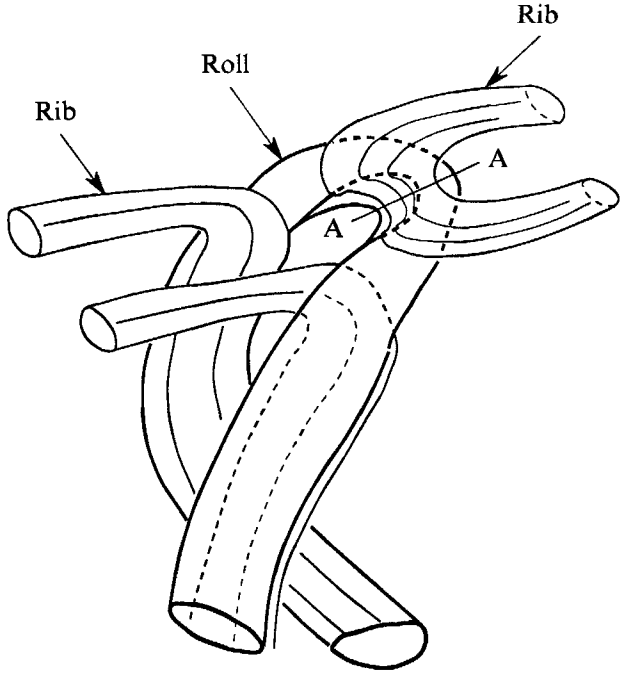

FIGURE 11. Constant $|\omega|$ surface plots (50% of peak value $|\omega|_p$) showing the evolution of three-dimensionality of the rolls and the formation of ribs (in numerical simulation) at $t^* = 2.4$, 3.2, 3.6, and 4.4. The views shown at each time are: (*a*) projection on the minor plane; (*b*, *c*) vorticity contours in the major and minor planes; (*d*) projection on the major plane; (*e*) isometric view; (*f*) schematic showing details of rib–roll interaction.

joins the roll from the high-speed side. The part of the rib which aligns with the roll in the azimuthal direction (i.e. the short segment across the section A–A in figure 11*f*) fuses with the latter by vorticity diffusion.

3.2.2. *Rib formation mechanism*

Generation of streamwise vorticity from an initial distribution of azimuthal vorticity becomes clear if we examine the coherent vorticity transport equation. A double decomposition,

$$f(\boldsymbol{x}, t) = f_c(\boldsymbol{x}, \tau) + f_r(\boldsymbol{x}, t),$$

yields the coherent vorticity transport equation as

$$\frac{D\boldsymbol{\omega}_c}{Dt} = \boldsymbol{\omega}_c \cdot \nabla \boldsymbol{u}_c + \frac{1}{Re} \Delta \boldsymbol{\omega}_c + \langle \boldsymbol{\omega}_r \cdot \nabla \boldsymbol{u}_r - \boldsymbol{u}_r \cdot \nabla \boldsymbol{\omega}_r \rangle, \tag{3.1}$$

where $D/Dt \equiv \partial/\partial t + \boldsymbol{u}_c \cdot \nabla$ is the material derivative following a fluid particle in the coherent flow field (see Hussain & Zaman 1980), and subscripts c and r designate the coherent and incoherent parts, respectively. To study the deformation of elliptic structures and the generation of braid streamwise vorticity, it is more revealing to use local coordinates along a vortex tube. A schematic of the initially undeformed elliptic rolls and a braid vortex tube along with the fixed Cartesian coordinate

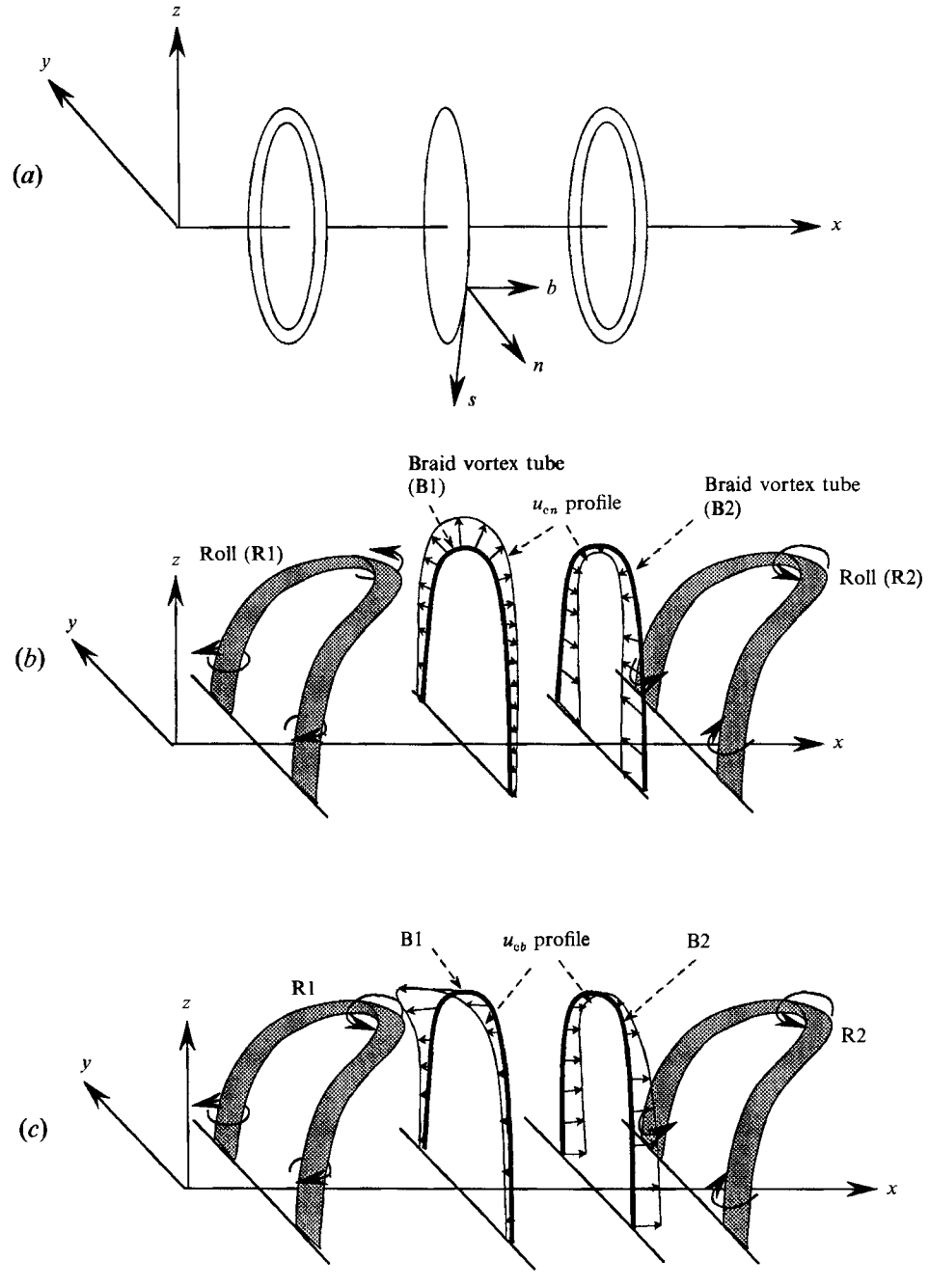

FIGURE 12(*a–c*). For caption see facing page.

(x, y, z) and local coordinate (s, n, b) definitions are shown in figure 12(*a*). Here, s, n and b refer to the coordinates in the tangential, normal and binormal directions.

For a high Reynolds number flow and in a region close to the jet exit where incoherent turbulence is very small, we may neglect the last two terms in (3.1) so that the vortex stretching term $\boldsymbol{\omega}_c \cdot \nabla \boldsymbol{u}_c$ is the major cause of any change in the coherent vorticity field.

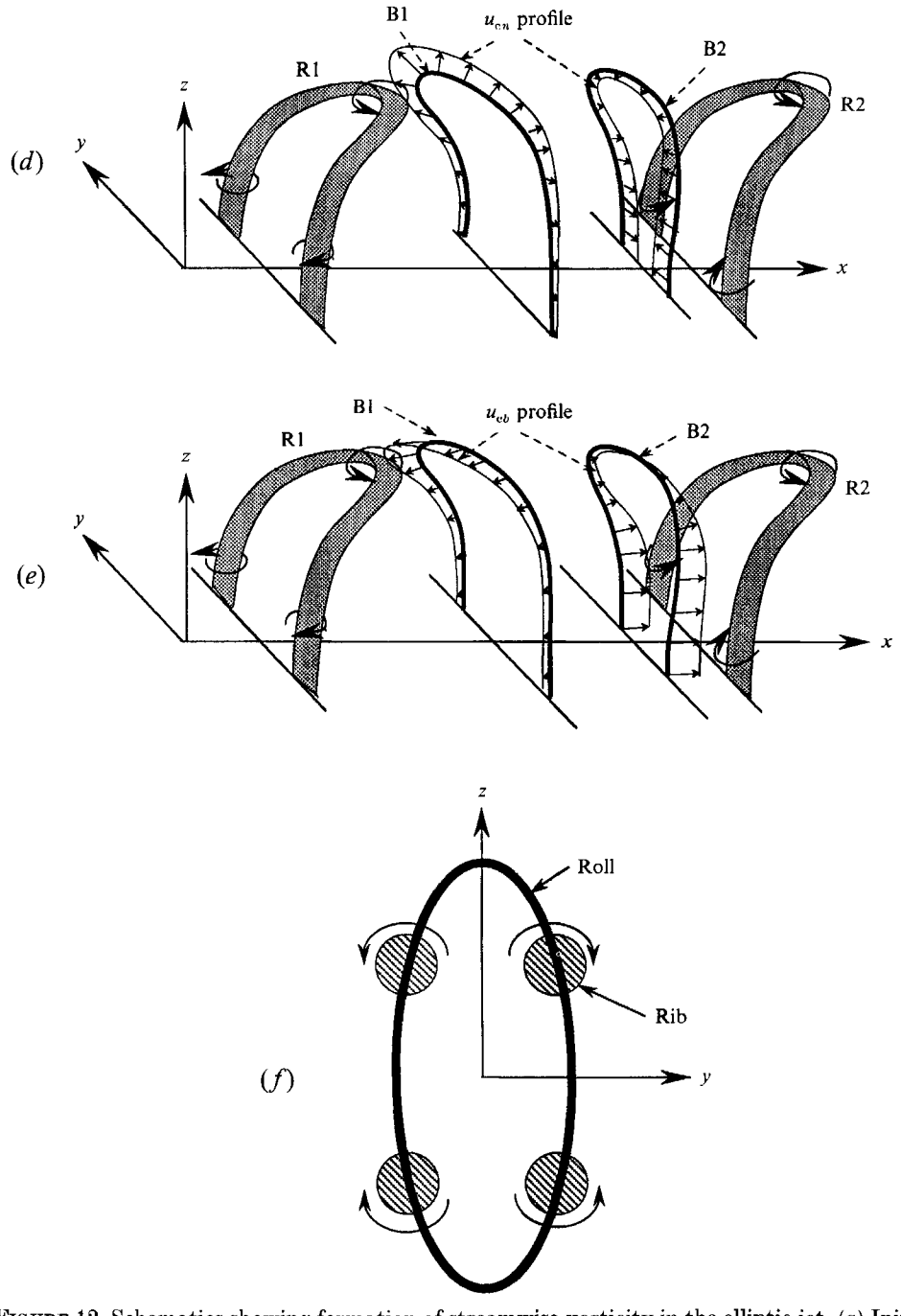

FIGURE 12. Schematics showing formation of streamwise vorticity in the elliptic jet. (*a*) Initial roll configurations and braid vortex before deformation. (*b*, *c*) Distributions of u_{cn} and u_{cb} along the undeformed braid vortex tubes induced by deformed rolls. (*d*, *e*) Deformation of braid vortex tubes by roll induction and the corresponding u_{cn} and u_{cb} distributions. (*f*) Schematic (front view) showing the locations of the ribs with respect to the roll.

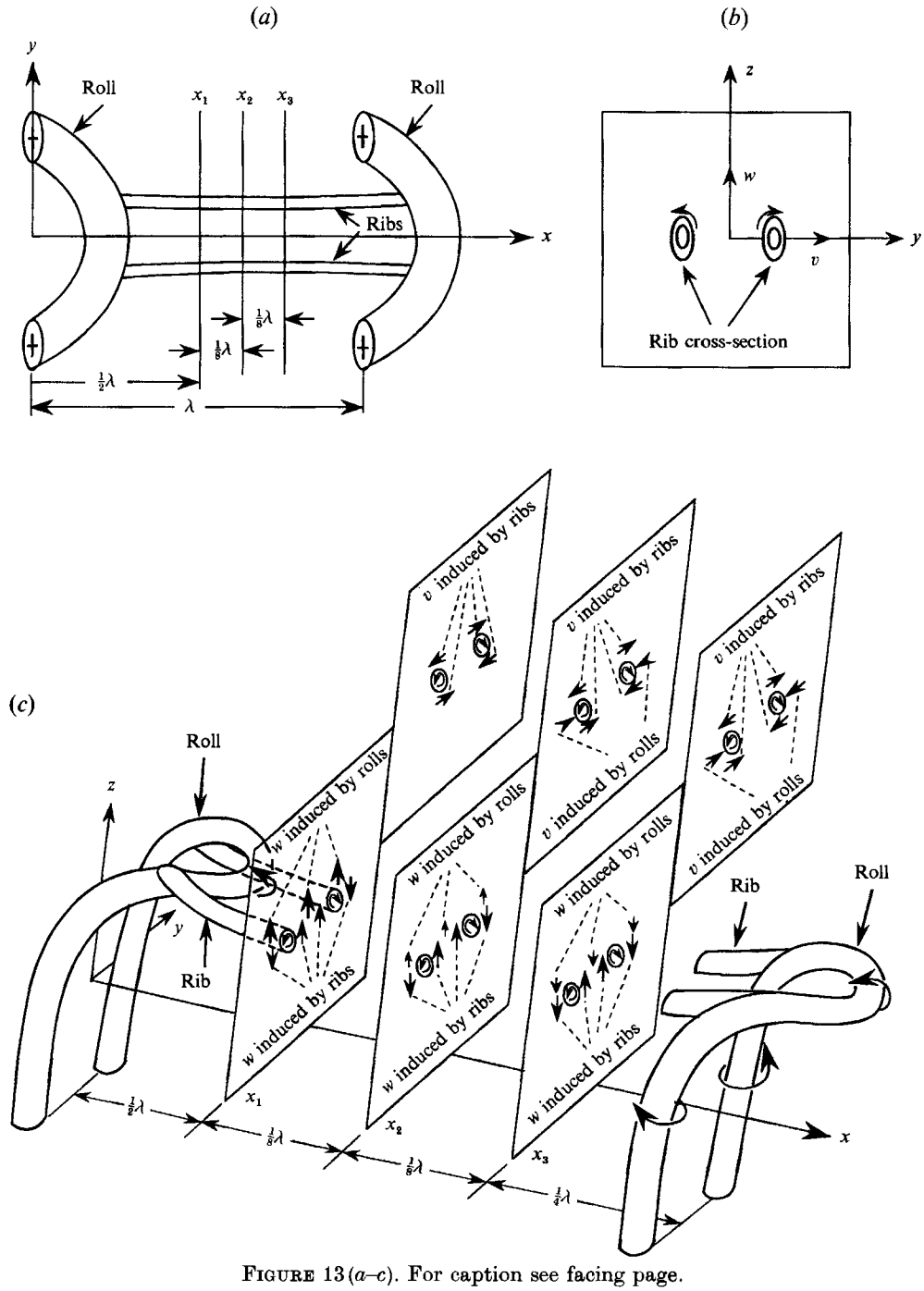

FIGURE 13(a–c). For caption see facing page.

As explained before, initially the major-axis side of a roll advects ahead of the minor axis side by self-induction, while the braid vortex tubes remain nearly planar due to their substantially lower circulation. Figure 12(b, c) shows schematically the induced normal and binormal velocity distributions (u_{cn} and u_{cb}) of the deformed rolls which are encountered by the nearly planar braid vortex tubes. Note that the

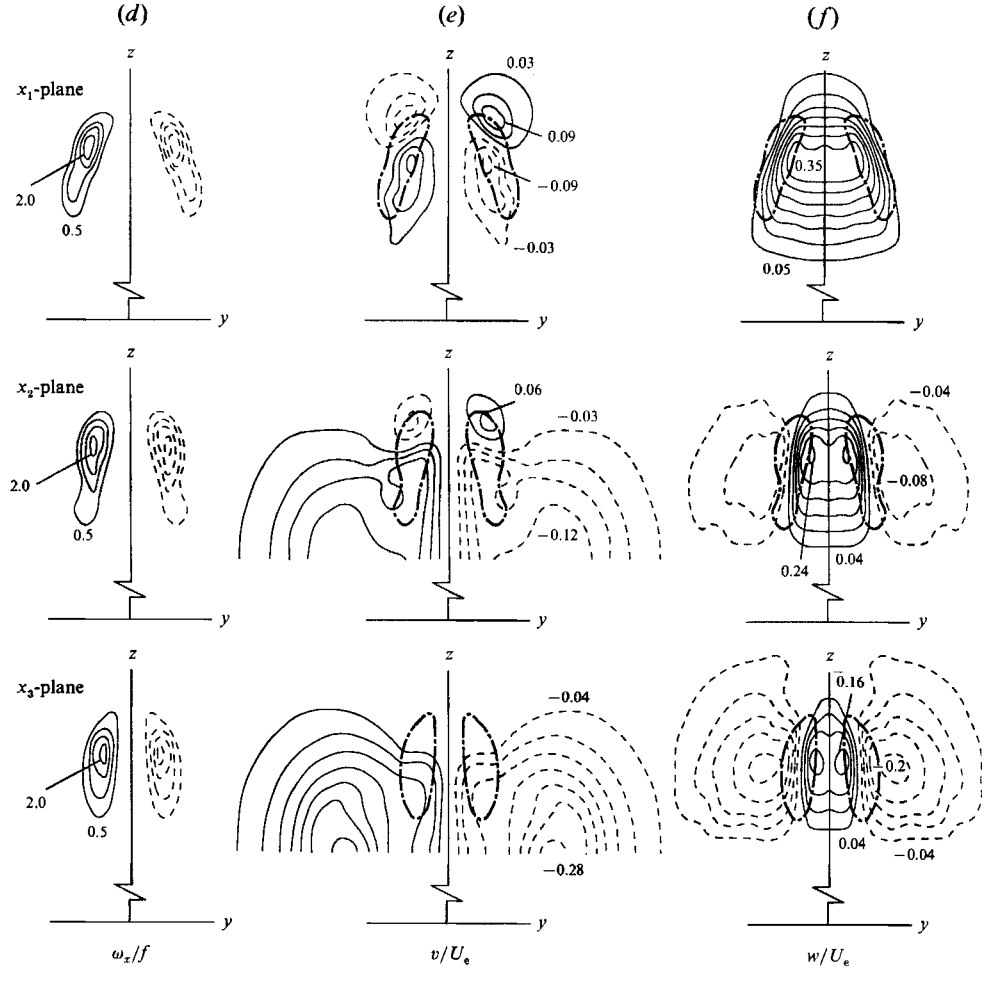

FIGURE 13. (*a*, *b*) Schematic of the coordinates in the numerical simulation. (*c*) Schematic of the velocity fields induced by ribs and rolls in three successive planes. Contours of (*d*) ω_x; (*e*) v; (*f*) w at three planes in the braid (shown in *a*) of the elliptic jet (numerical simulation).

velocity distributions shown in figure 12 are drawn in a frame moving with each tube. Braid vortex tube B1, being close to the upstream roll R1, is subject to an outward normal velocity component, while vortex tube B2, which is closer to the downstream roll R2, is subject to an inward normal component. Furthermore, the major-axis side of B1 is pushed radially outward more than the minor-axis side because of greater u_{cn} here due to closer proximity to the roll's major-axis side. For the same reason, the minor-axis side of B2 is pushed radially inward more than its major-axis side. Simultaneously, vortex tube B1 is subject to a negative u_{cb} field, while vortex tube B2 experiences positive u_{cb}. Similar to the u_{cn}-field, the magnitude of u_{cb} is higher in the major-axis side of B1, while it is higher in the minor-axis side of B2. As a result of the velocity gradient $\partial u_{cb}/\partial s$, the major-axis side of B1 falls behind its minor-axis side, while the minor-axis side of B2 moves ahead of its major-axis side in the downstream direction. The net effect is to tilt the major-axis sides of both B1 and B2 upstream relative to their respective minor-axis sides (figure 12*d*, *e*). Once a segment of the braid vortex tubes is locally tilted in the streamwise direction, ω_s is further

augmented by the strain field $\partial u_{cs}/\partial s$ (due to induction of corotating rolls at the saddle). Note that in a (y,z)-plane, the sense of the braid streamwise vorticity is opposite in neighbouring quadrants. The like-signed vorticity filaments in each quadrant bundle up together to form the streamwise rib vortex. The locations of the ribs with respect to a roll are schematically shown in figure 12(f).

In contrast, studies of plane shear layers (Lasheras, Cho & Maxworthy 1986; Lasheras & Choi 1988; Lee, Metcalfe & Hussain 1991) and circular jets (Martin & Meiburg 1991) show that three-dimensional perturbations grow very fast in the braid, generating ribs which then interact with the spanwise rolls to induce their three-dimensionality. Rogers & Moser (1992) have shown that rib formation and spanwise roll undulations are a manifestation of the translative instability, identified by Pierrhumbert & Widnall (1982). Interestingly, in the elliptic jet the sequence of streamwise vorticity generation appears to be opposite to that in a plane shear layer and a circular jet; that is, roll deformation precedes the rib formation here.

Because of the intrinsic azimuthal mode $m = 2$, the elliptic jet does not require any imposed azimuthal perturbation for the development of three-dimensionality and subsequent rib formation. In contrast, a circular jet requires the imposition of an azimuthal perturbation for three-dimensional development (Martin & Meiburg 1991; Melander *et al.* 1991). Spatially localized ribs may cause the coherent vorticity and velocity fields of the elliptic jet to differ significantly from the circular jet because its ribs are not fixed in space (unless they are forced to be spatially fixed, as in the study of Meiburg & Lasheras 1988).

3.2.3. *Vorticity and velocity fields of the ribs*

The streamwise vorticity ω_x and transverse velocities v and w in the braid have been studied at three streamwise locations using numerical simulation. The coordinates and the measurement planes (x_1, x_2, x_3) along with the relative locations of the rolls are shown schematically in figure 13(a,b). Note that the x_1-plane lies midway between the minor-axis sides of the upstream and downstream rolls, while the planes x_2 and x_3 lie downstream of the x_1-plane at intervals $\frac{1}{8}\lambda$ (see figure 13a). The x_1-, x_2-, and x_3-planes are drawn with disproportionate spacing for enhancing clarity in figure 13(c).

Let us first examine the downstream variation of rib and roll induction in a (y, z)-plane. This is shown schematically in figure 13(c); here the direction of induced velocities v and w in successive planes (x_1, x_2, x_3) are shown by arrows. One would expect that the velocity induced by the ribs in these successive planes should be very similar, while that induced by the rolls should change significantly as one moves toward the downstream roll. Since the x_1-plane is closer to the major-axis side of the upstream roll, the $+w$ induced by this roll should be stronger than that ($-w$) from the downstream roll. A superposition of the w-velocities induced by the rolls and ribs results in substantial $+w$ between the ribs, but because of cancellation there should be very little $+w$ outside (azimuthally) the rib pair. Farther downstream, $+w$ induced by the upstream roll diminishes, while $-w$ induced by the downstream roll increases. As a result, the peak in $+w$ decreases between the ribs, and the peaks in $-w$ increase outside the rib pair.

Note that both the rolls and ribs contribute to the induced v-field. Thus in the midplane (i.e. x_1 plane), the v-component induced by the upstream and downstream rolls approximately cancel each other; the v-field in this plane is due primarily to rib induction. With increasing streamwise distance, the effect of unbalanced roll induction on the v-field is to increase the peak in the regions outside the rib pair and

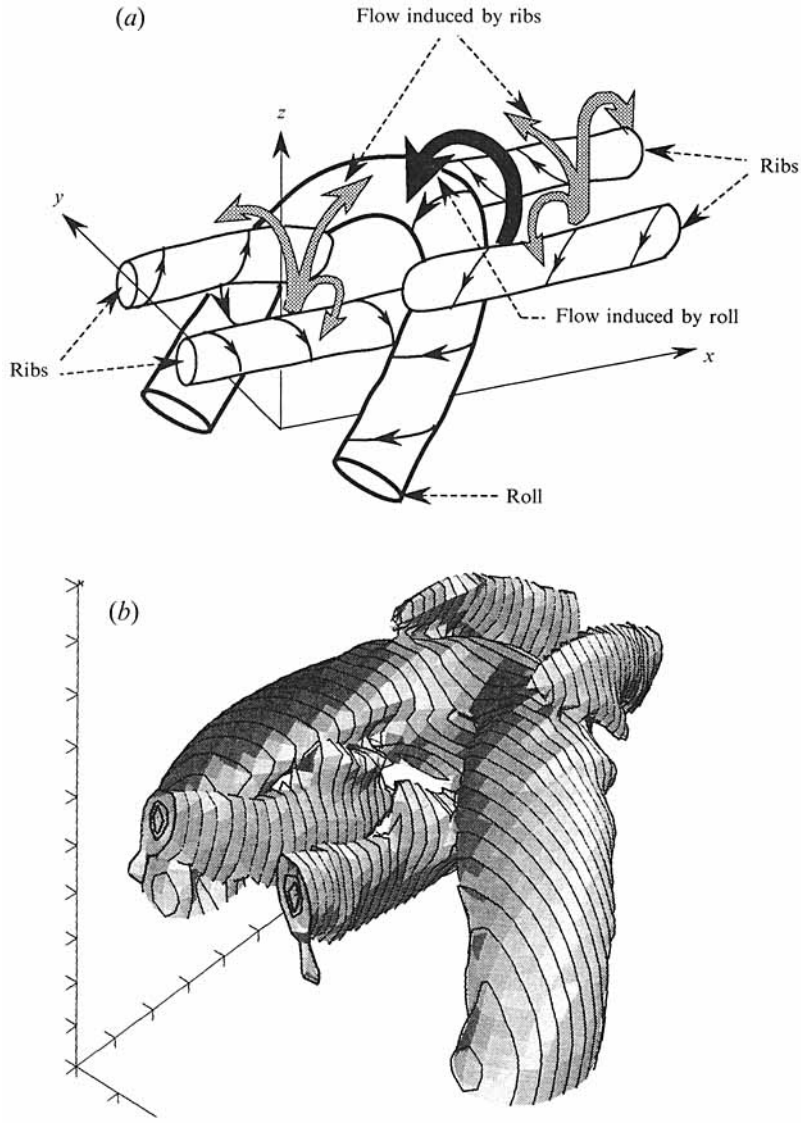

FIGURE 14. (*a*) Schematic showing the ejection and engulfment of fluid due to rib–roll interaction. (*b*) Isovorticity surface (numerical simulation) showing the major-axis side of the structure where the ribs join with the roll.

closer to the jet axis, and the induced v by the ribs and the rolls tends to cancel on the zero-speed side.

Contours of the streamwise component of vorticity ω_x and transverse velocities v and w obtained via numerical simulation are shown in figure 13(*d–f*) at the three locations defined in figure 13(*a, c*) (one ω_x contour is superposed as a chain-link line in figure 13(*e,f*) for common reference among (*d–f*)). The transverse velocities v and w exhibit significant differences in these three planes, as expected. At x_1, v-contours show positive and negative regions across the rib cross-sections due to their own induction, as anticipated in figure 13(*c*). With increasing x, the induced outward velocity field of the minor-axis side of the upstream roll decreases, but the radially

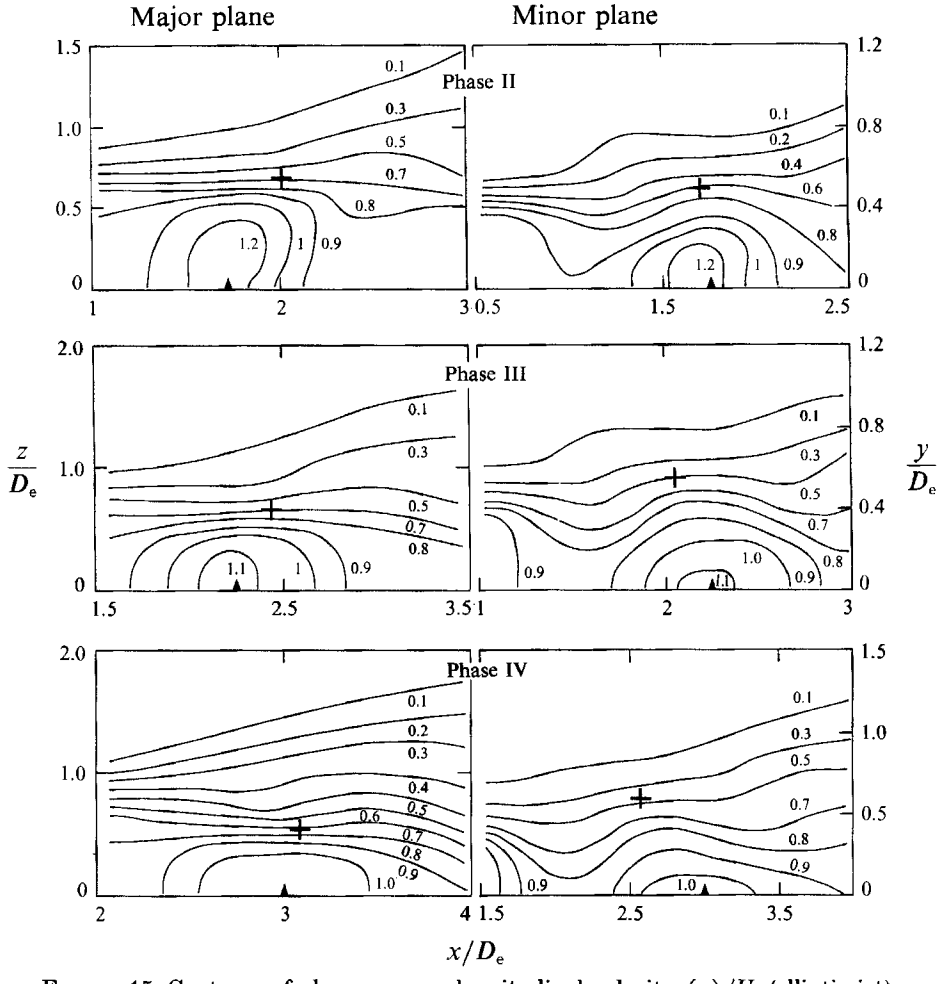

FIGURE 15. Contours of phase-average longitudinal velocity $\langle u \rangle / U_e$ (elliptic jet).

inward velocity due to the downstream roll increases. As a result, outward radial motion above the ribs is suppressed, while inward motion is augmented (both in area and magnitude) below the ribs. Since the w-component of velocity induced by the roll is positive at x_1, it adds positive w between the ribs and cancels negative w on the outer regions. Because the negative component of w induced by the downstream roll increases as we move downstream, the contours of w around the ribs show the development of stronger and larger regions of negative w (i.e. radially inward in the z-direction) as x increases.

The contours of w shown in figure 13(f) reveal that the outward ejection is strongest near the downstream side of a preferred mode structure (x_1-plane), while the inward ingestion is strongest near the upstream side (x_3-plane). The mechanism of such ejection and ingestion of fluids due to rib and roll induced motions on the major-axis side is shown schematically in figure 14(a). For comparison, a constant vorticity surface on the major-axis side at $t^* = 4.4$ is presented in figure 14(b), showing the joining of the ribs with the roll. In figure 14(a), the directions of the fluid motion induced by the rolls and the ribs are shown by solid and dot-filled arrows, respectively. On the downstream side of the roll, the outward radial motion induced

by the ribs reinforces the motion induced by the roll, thus producing a stronger outward ejection of jet fluid there. On the upstream side, the induced motion of the ribs opposes the inward roll-induced motion, thereby decreasing it and causing downstream ejection to be stronger than upstream ingestion. This simplified schematic is consistent with the measured and simulated contours of $\langle v \rangle$ (figure 16*a–c*), which show a positive region at the front and a smaller negative region with a lower peak value at the back of the roll. This is further discussed in the following section. Energetic vortical fluid ejection and subsequent slow ingestion was noted in circular jets (Hussain & Clark 1981).

3.3. *Other phase-average properties*

In this section we present a limited amount of the phase-averaged data, i.e. only for three phases (e.g. II, III and IV), but our discussion includes consideration of data at the other two phases (I and V) also. These data can be used for technological purposes and to validate numerical studies of the elliptic jet preferred mode structure. In all figures, vortex centres are identified by a + for spatial reference.

3.3.1. *Longitudinal and transverse velocities*

Phase-average longitudinal and transverse velocity contours $\langle u \rangle / U_e$ and $\langle v \rangle / U_e$ are shown in figures 15 and 16(*a*) respectively. Near the jet axis, the roll's induced motion coincides with the flow direction, producing a peak in the $\langle u \rangle$ distribution which is higher than the mean exit velocity. Since an elliptic structure undergoes deformation, the induction from the major- and minor-axis sides produce a peak in $\langle u \rangle$ near the jet axis at a streamwise location which lies upstream of the vortex centre in the major plane, but downstream of the vortex centre in the minor plane. Contour patterns of $\langle u \rangle$ in the circular jet (not shown) are qualitatively similar to those in the minor plane except that the peak in $\langle u \rangle$ occurs near the jet axis almost at the same axial location as that of the vortex centre because in this case the roll remains planar.

Hussain & Zaman (1981) have discussed that the flow reversal on the zero-speed side causes a dip in the measured vorticity contours. In the present case, low-level vorticity contours in the circular jet (phase III and IV) and in the minor plane of the elliptic jet (phases I–III) indeed show a mild dip, indicating the possibility of flow reversal, but no such dip is present in the major-plane vorticity contours (see figure 4*a*). Distributions of $\langle u \rangle$ reveal that the vortex centres in the major plane of the structure acquire a higher advection velocity (about $0.7\,U_e$) than that in the minor plane or in the circular jet (about $0.5U_e$) because of stronger self-induced motion. This higher structure advection velocity and the absence of any significant dip in the $\langle \omega \rangle$-contours suggests that flow reversal is insignificant on the major-axis side.

The contours of $\langle v \rangle$ (figure 16*a*) show stronger outward fluid ejection (i.e. $+\langle v \rangle$) at the front of a vortical structure than inward motion (i.e. $-\langle v \rangle$) at its back at all phases and in both planes. Both outward and inward motions in the major plane are as strong or stronger than the corresponding motions in the minor plane. As discussed in §3.2.2, this is because the ribs downstream of the major-axis sides induce $+v$ in addition to that induced by the roll, thus producing a higher peak in $+\langle v \rangle$ on the roll's downstream side than the $-\langle v \rangle$ peak on its upstream side. Furthermore, the $\langle v \rangle$-distribution in the major plane is influenced by the inward self-induced motion of the structure here. Such inward motion may be the reason for a higher $-\langle v \rangle$ peak in this plane at phase IV.

At later phases, contours of $\langle v \rangle$ in both planes of the elliptic jet (figure 16*a*) are

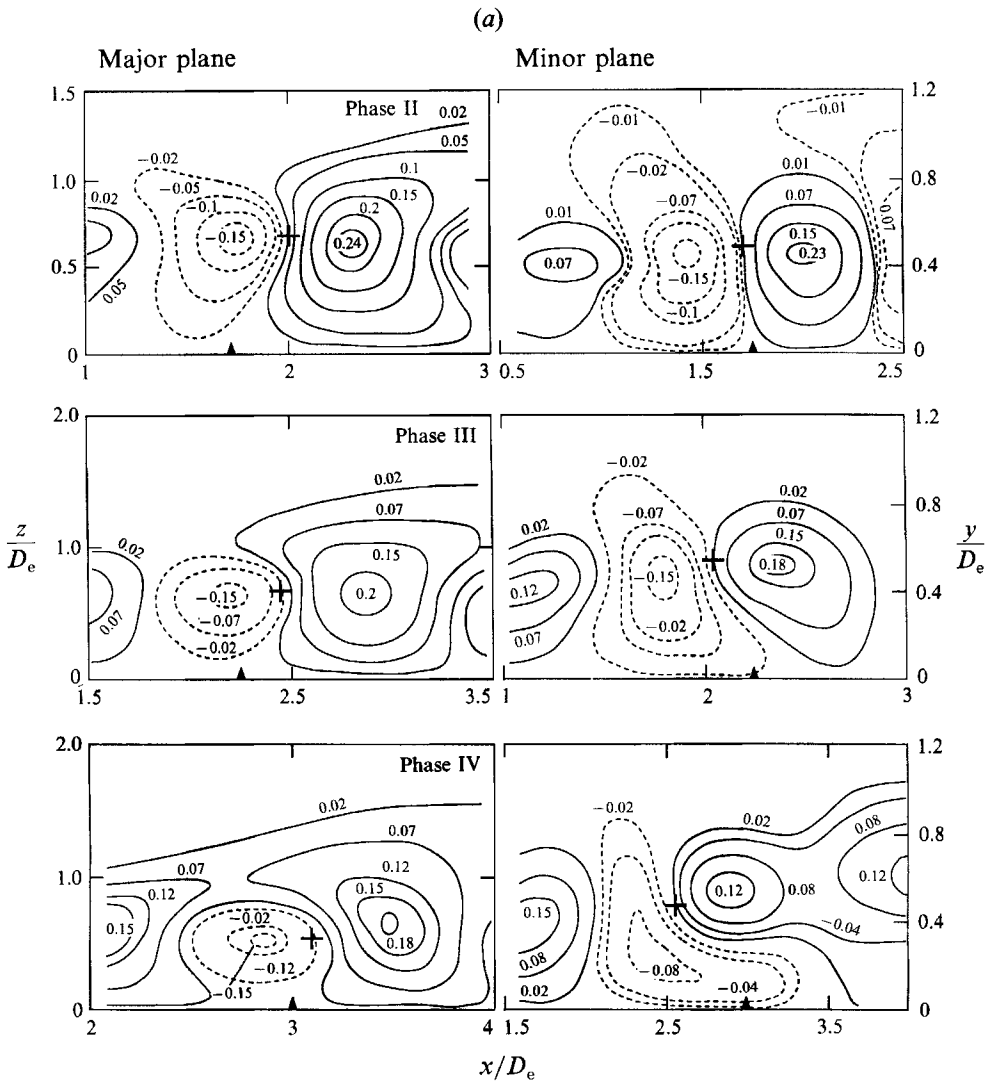

FIGURE 16(a). For caption see facing page.

quite different from those in the circular jet (figure 16*b*). Evidently, the late time spatial distributions of $\langle v \rangle$ are sensitive to roll deformation as well as induction by ribs. In the circular jet, the vorticity distributions are fairly symmetric about the vortex centre in the streamwise direction, resulting in symmetric $\langle v \rangle$-contours. Asymmetric distributions of $\langle \omega \rangle$ on the high- and zero-speed sides of the minor and major planes, respectively, produce asymmetric $\langle v \rangle$-contours in these regions. For example, negative contours in the minor plane (phases III and IV) extend toward the downstream side of the structure centre near the jet axis. In the major plane, the S-shaped fold in the vorticity contour produces $\langle v \rangle$ distributions that are quite different at later phases from those in the minor plane or in the circular jet. For example, positive contours in the major plane extend upstream on the zero-speed side. In addition, the v-patterns from the numerical simulation data at $t^* = 4.4$ and 4.8 (figure 16*c*) are quite similar to those obtained experimentally (figure 16*a*, phases III and IV).

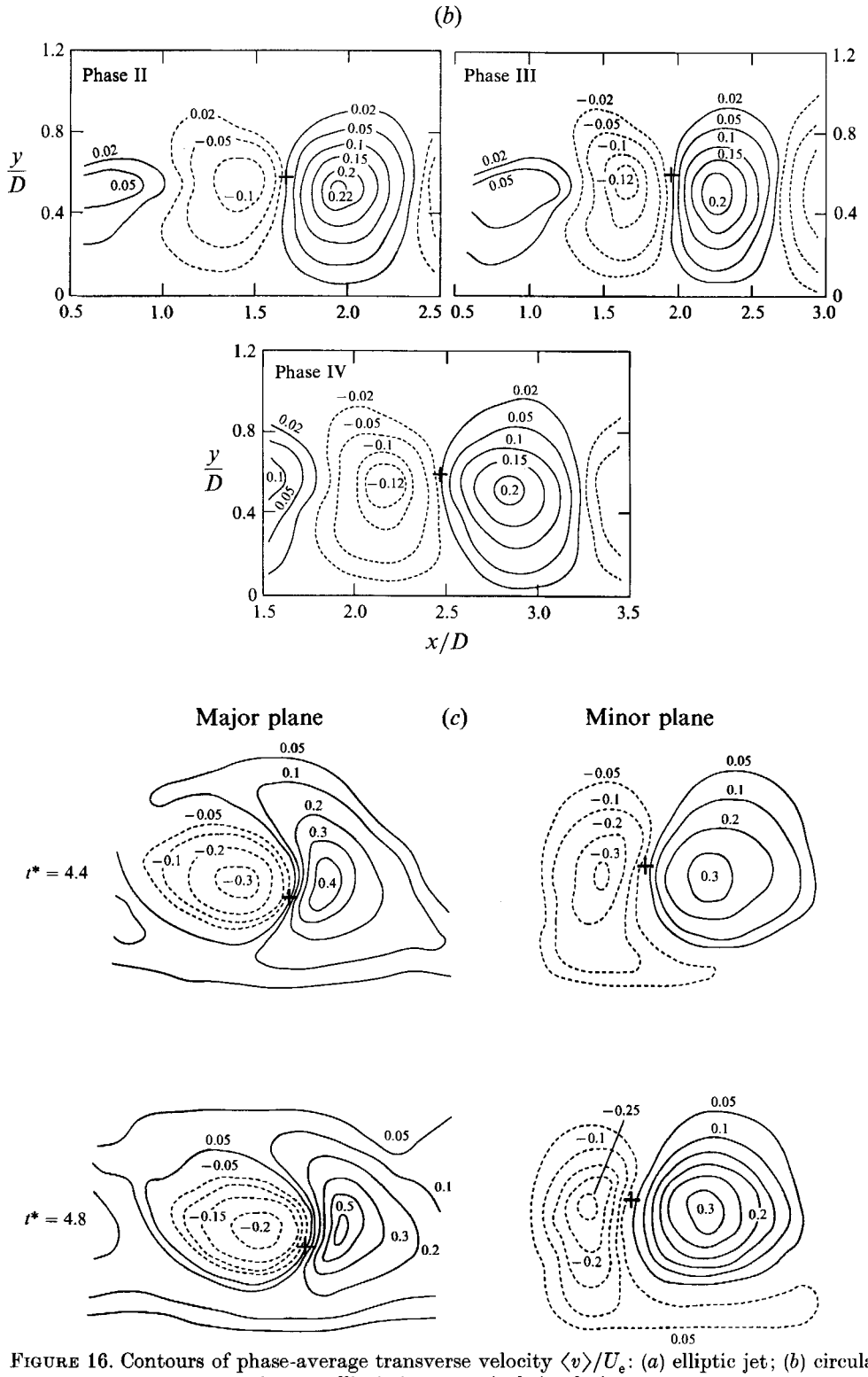

FIGURE 16. Contours of phase-average transverse velocity $\langle v \rangle / U_e$: (*a*) elliptic jet; (*b*) circular jet; (*c*) elliptic jet numerical simulation.

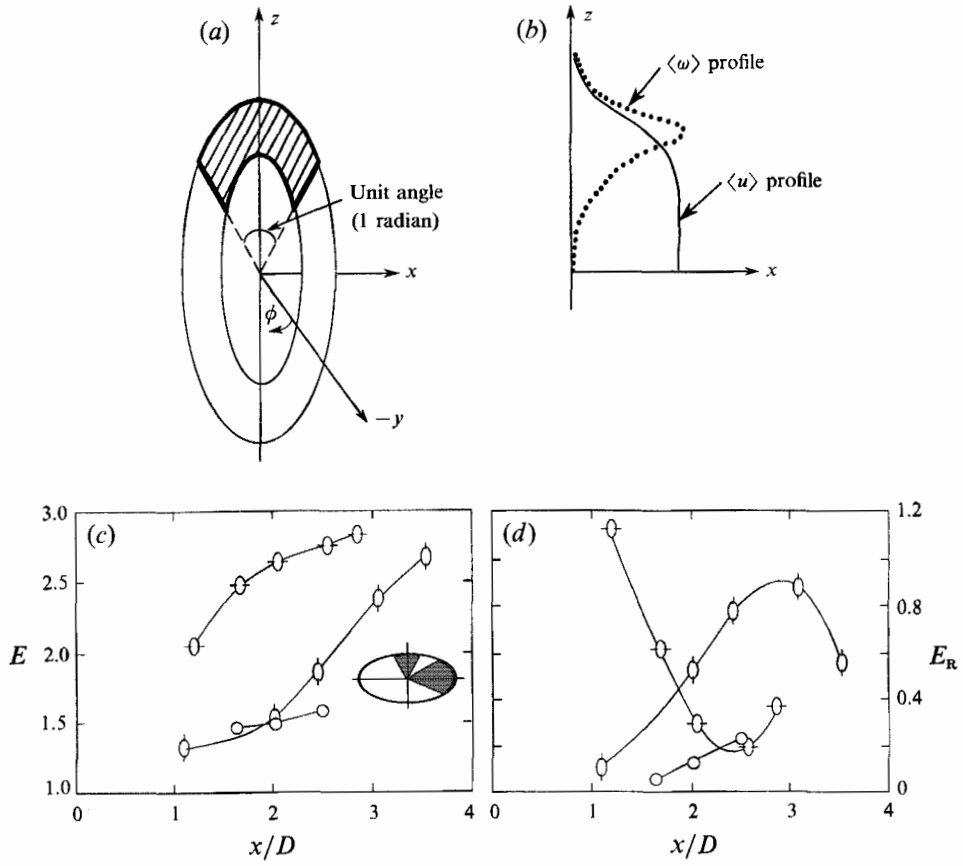

FIGURE 17. (*a*) Schematic showing the method of volume flux calculation. (*b*) Qualitative distributions of $\langle u\rangle$ and $\langle\omega\rangle$ in the transverse direction. (*c, d*) Axial variations of non-dimensional entrainment $E(x')$ and entrainment rate $E_R(x')$ during preferred mode structure evolution in the elliptic and circular jets. ⟨⟩, major plane; ⟨⟩, minor plane; ○, circular jet.

3.3.2. *Mass entrainment*

Traditionally, the volume flux $Q(x')$ at a given streamwise location is obtained by integrating the mean velocity profile $U(y)$; here $x' = x/D$ is the non-dimensional streamwise location. Integration starts from the jet centreline (i.e. $y = 0$; $z = 0$) and the limit of integration on the zero-speed side is usually taken to be the point where the mean velocity reaches a certain percentage (i.e. threshold level) of the local centreline velocity. Alternatively, one can fit an appropriate curve to $U(y)$ such that $U \to 0$ as $y \to \infty$ and integrate up to $y = \infty$. These steps are to minimize the adverse effects of high fluctuation intensity and possible flow reversal on the hot-wire data. Non-dimensional entrainment $E(x')$ and entrainment rate $E_R(x')$ are defined as

$$E(x') = \frac{Q(x')}{Q_0} \quad \text{and} \quad E_R(x') = \frac{\mathrm{d}E(x')}{\mathrm{d}x'},$$

where Q_0 is the volume efflux at the exit plane. A measure such as $E(x')$, based on the time-average velocity data, overestimates the amount of entrainment because it includes both vortical and non-vortical fluids flowing downstream (see Ricou &

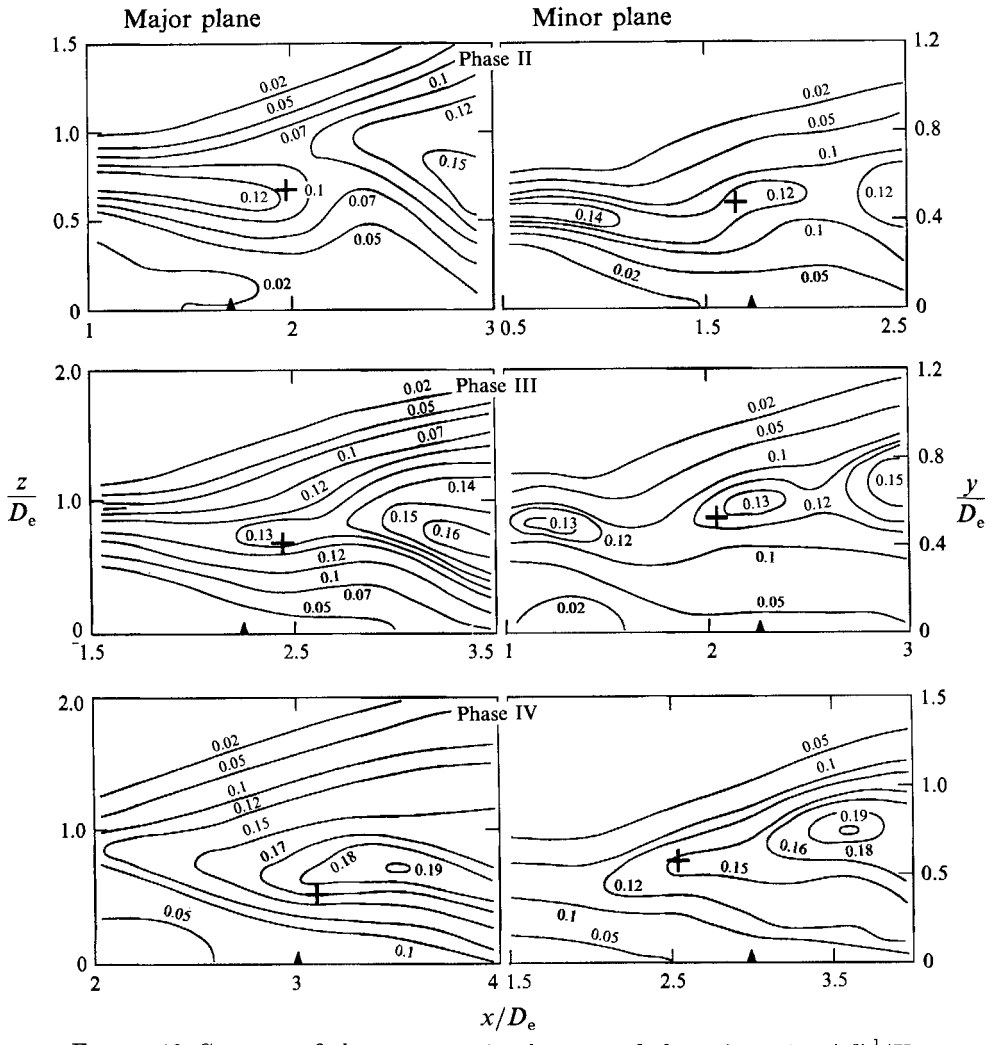

FIGURE 18. Contours of phase-average incoherent turbulence intensity $\langle u_r^2 \rangle^{\frac{1}{2}}/U_e$.

Spalding 1961). We define entrainment as acquisition of vorticity by ambient irrotational fluid and thus prefer to base the definition on vortical fluid efflux only. The entrainment of vortical fluid during preferred mode structure evolution was calculated in both planes from the $\langle u \rangle(y)$ and $\langle u \rangle(z)$ data through the structure centre at each phase. The limits of integration are set rather subjectively to be the location where the vorticity $\langle \omega \rangle$ decays to 5% of its peak. This location is obtained by extrapolating the $\langle \omega \rangle$ profile using an exponential decay curve fit through data at higher $|\omega|$.

In the present study, since we have velocity data only in the major and minor planes, local volume fluxes were calculated through sectors that make a unit angle (i.e. 1 radian) on both the major- and minor-axis sides (i.e. volume flux due to a curved roller-like structure per unit subtended angle). This method of volume flux estimation and the distributions of $\langle u \rangle(z)$ and $\langle \omega \rangle(z)$ are shown schematically in figure 17 (*a*, *b*). The entrainment $E(x')$, computed from the measured distributions of $\langle u \rangle(y)$ and $\langle u \rangle(z)$, and entrainment rate $E_R(x')$ are shown in figure 17 (*c*, *d*)

respectively. To compare mass entrainment in the major- and minor-axis sides of an elliptic jet, a reference Q_0 needs to be defined properly. Similar to $Q(x')$, Q_0 is defined as the jet exit volume flux through an area subtended by a unit angle (one radian) on the major- or minor-axis side, as appropriate (shown as inserts in figure 17*c*). In these figures, $E(x')$ and $E_R(x')$ for the circular jet are also included.

Within our measurement range, $E(x')$ in the minor plane is considerably higher than that in the major plane. At phase I, the vorticity gradient across the structure in the minor plane is almost twice that in the major plane, thus producing greater entrainment by vorticity diffusion. The vorticity distribution is more diffuse in the major plane, presumably due to incomplete rollup of the vorticity sheet. However, at later phases, an increase in the surface area due to fold formation and the engulfment of fluid between the rib and the roll and subsequent diffusion of vorticity to this fluid increase $E_R(x')$ significantly in the major plane. Additionally, an increase in the roll perimeter in the elliptic jet (about 10% between phases I and IV; see §3.1.3) indicates the presence of vortex stretching which should increase entrainment via vorticity diffusion. $E(x')$ in the circular jet is close to that of the major plane up to phase II; farther downstream, both $E(x')$ and $E_R(x')$ become substantially higher in the major plane. The time-average volume flux measures of Ho & Gutmark (1987) in an unexcited elliptic jet also show higher values of $E(x')$ in the minor plane than in the major plane. Their results show a linear increase in volume flux with x/D_e over a longer axial distance. This is not unexpected because they include irrotational fluid in their measurements. In addition, time-averaging smears detailed events that occur at each phase.

In summary, both $E(x')$ and $E_R(x')$ in the elliptic jet (average of major- and minor-axis sides) are much higher than those of the circular jet, indicating substantially more effective mass entrainment in the elliptic jet.

3.3.3. *Turbulence intensities and Reynolds stresses*

Phase-average incoherent turbulence intensities $\langle u_r^2\rangle^{\frac{1}{2}}/U_e$ and $\langle v_r^2\rangle^{\frac{1}{2}}/U_e$ are shown in figures 18 and 19, respectively. Contours of $\langle u_r^2\rangle^{\frac{1}{2}}$ in the major and minor planes are quite dissimilar; the peak value of $\langle u_r^2\rangle^{\frac{1}{2}}$ is higher in the major plane, and as in the minor plane, the peak in $\langle u_r^2\rangle^{\frac{1}{2}}$ does not occur near the structure centre. The contour patterns of $\langle v_r^2\rangle^{\frac{1}{2}}$ are similar in both planes, and the peak occurs near the structure centre. At each phase, the peak values of $\langle u_r^2\rangle^{\frac{1}{2}}$ and $\langle v_r^2\rangle^{\frac{1}{2}}$ are higher in the elliptic jet than in the circular jet (not shown). In the elliptic jet, higher levels of incoherent turbulence presumably cause the peak coherent vorticity to decay faster in the elliptic jet (figure 7). For comparison with corresponding time-average contours of r.m.s. u- and v-fluctuations (for both unexcited and excited cases) see figures 27 and 28, respectively.

The peaks of $\langle u_r v_r\rangle$ occur approximately at the saddles of $\langle\omega\rangle$ (figure 20*a*). This type of relation between vorticity and incoherent Reynolds stress distributions is similar to that observed in other flows, namely circular jets (Hussain & Zaman 1980), wakes (Cantwell & Coles 1983; Hayakawa & Hussain 1985) and mixing layers (Metcalfe *et al.* 1987). The generation of $\langle u_r v_r\rangle$ at the saddle (or braid) due to the stretching of ribs by the induced motions of neighbouring rolls has been discussed in detail in Part 2.

The $\langle u_r v_r\rangle$-contours in the circular jet are qualitatively similar to those in the minor plane of the elliptic jet at phase II, and are therefore not shown (see Hussain & Zaman 1981). However, the peak values of $\langle u_r v_r\rangle$ in the elliptic jet, especially at later phases, are higher than those in the circular jet, implying greater momentum transport and turbulence production by incoherent Reynolds stress.

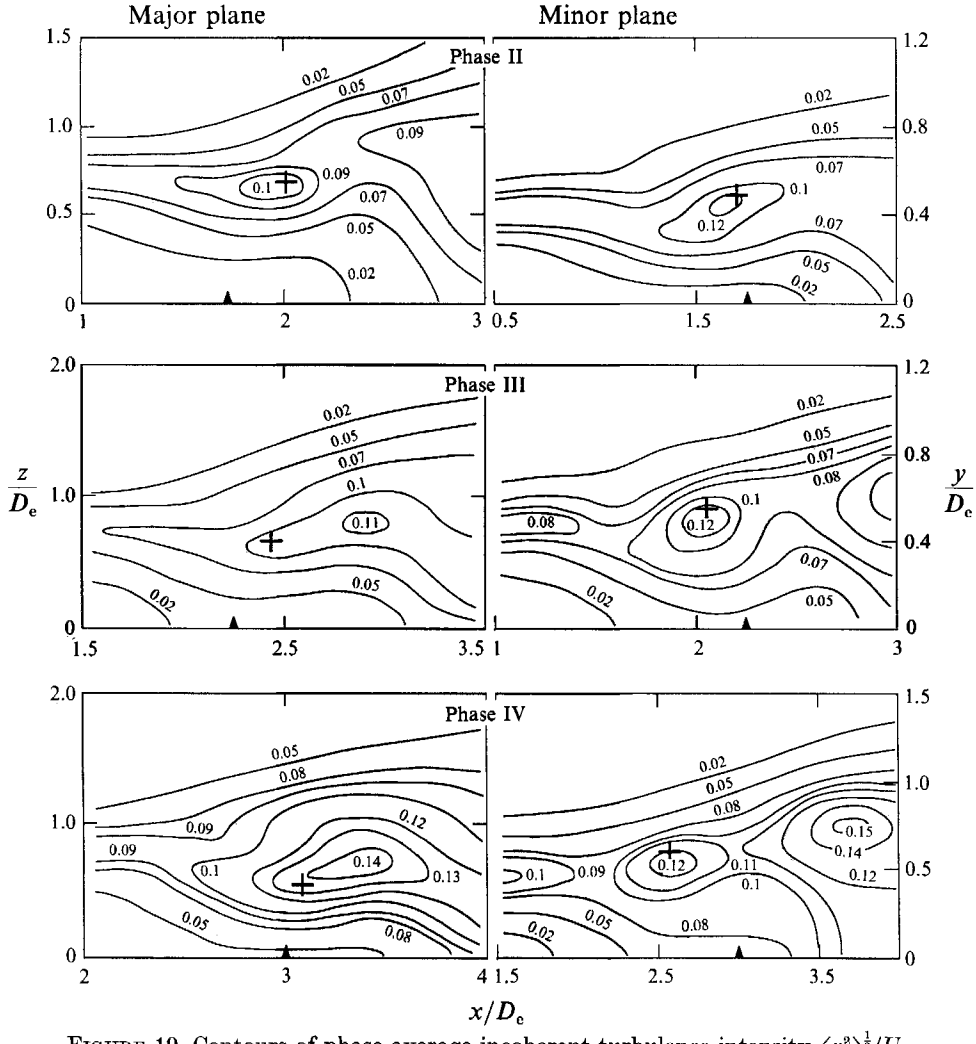

FIGURE 19. Contours of phase-average incoherent turbulence intensity $\langle v_r^2 \rangle^{\frac{1}{2}}/U_e$.

During the early phases of structure evolution, the transport of momentum by coherent Reynolds stress $\langle u_p v_p \rangle$ [$\equiv \langle (\langle u \rangle - U)(\langle v \rangle - V) \rangle$] is more significant than that by $\langle u_r v_r \rangle$. Contours of $\langle u_p v_p \rangle / U_e^2$ at phase II are shown in figure 20(*b*); distributions of $\langle u_p v_p \rangle$ at other phases are qualitatively similar, except that at later phases the peak values decrease. At phases IV and V, the values of $\langle u_r v_r \rangle$ and $\langle u_p v_p \rangle$ become comparable, indicating that the transports by incoherent and coherent Reynolds stresses become equally significant with increasing x.

Note that the $\langle u_p v_p \rangle$ contours are quite different in the two planes. In the minor plane, the contours exhibit alternate positive and negative regions, which are similar to those in a circular jet. This occurs because the structure ejects core fluid at its front and ingests ambient fluid at its back. Such x-periodicity of $\langle u_p v_p \rangle$ has been explained by Hussain & Zaman (1981) for the circular jet. However, in the major plane the inward advection of the vortex core produces negative $\langle u_p v_p \rangle$ (i.e. counter-gradient momentum transport) near the jet axis, while the outward motion of low-vorticity fluid produces positive $\langle u_p v_p \rangle$ on the zero-speed side.

At earlier phases, the positive peaks of $\langle u_p v_p \rangle$ in the minor plane are greater than

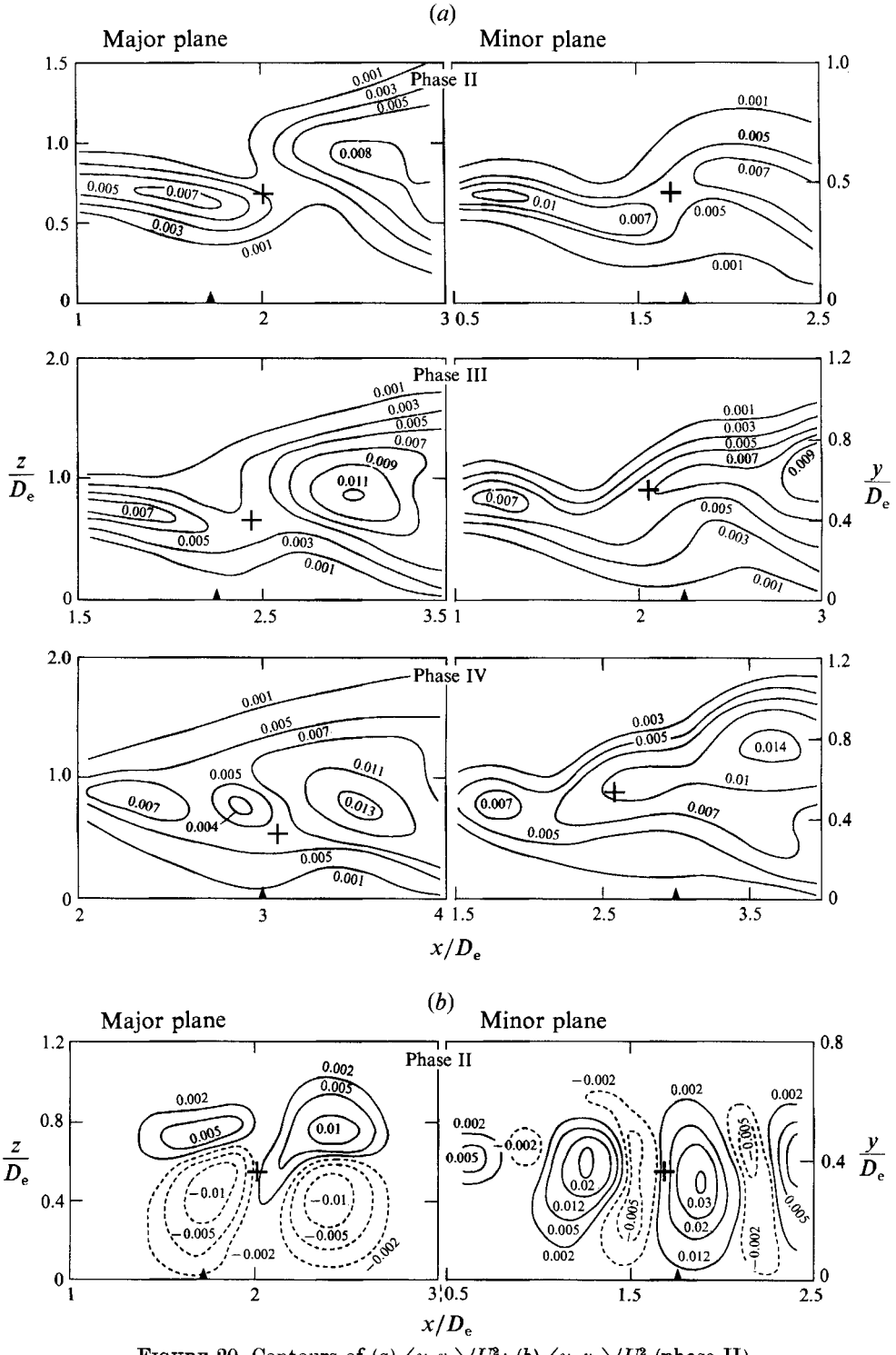

FIGURE 20. Contours of (a) $\langle u_r v_r \rangle / U_e^2$; (b) $\langle u_p v_p \rangle / U_e^2$ (phase II).

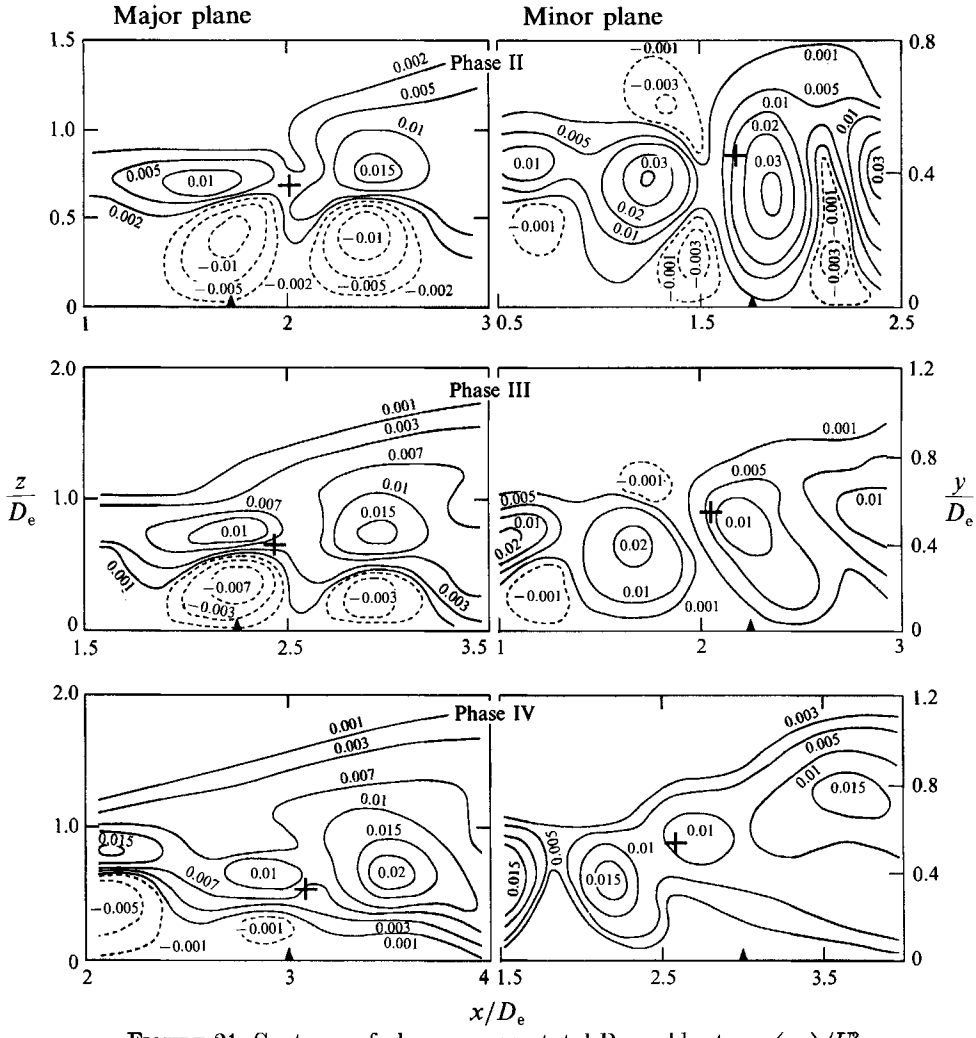

FIGURE 21. Contours of phase-average total Reynolds stress $\langle uv\rangle/U_e^2$.

the corresponding peaks in the major plane, while the negative peaks show an opposite trend. Also, during phases I–III, the area encompassed by a negative contour (say, $\langle u_p v_p\rangle/U_e^2 = 0.005$) is larger in the major plane than in the minor plane. This shows that at earlier phases, counter-gradient transport of momentum due to coherent motions is much greater in the major plane than in the minor plane.

Phase-average Reynolds stress $\langle uv\rangle/U_e^2[\equiv \langle u_r v_r\rangle/U_e^2 + \langle u_p v_p\rangle/U_e^2]$ is shown in figure 21. Not totally surprisingly, these contours show that the turbulent transport of momentum is mostly positive in the minor plane, while regions of strong counter-gradient transport are present in the major plane because of the structure's self-induced inward motion in this plane. While $+\langle uv\rangle$ is higher in the minor plane than in the major plane in phase I, they tend to be comparable in phase IV.

3.3.4. *Coherent turbulence production*

The phase-average production of turbulence by incoherent shear and normal stresses $\langle u_r v_r\rangle$, $\langle u_r^2\rangle$ and $\langle v_r^2\rangle$ is examined using the shear and normal production terms $\langle P_s\rangle[\equiv -\langle u_r v_r\rangle(\partial\langle v\rangle/\partial x + \partial\langle u\rangle/\partial y)]$ and $\langle P_n\rangle[\equiv (\langle P_{nu}\rangle + \langle P_{nv}\rangle) =$

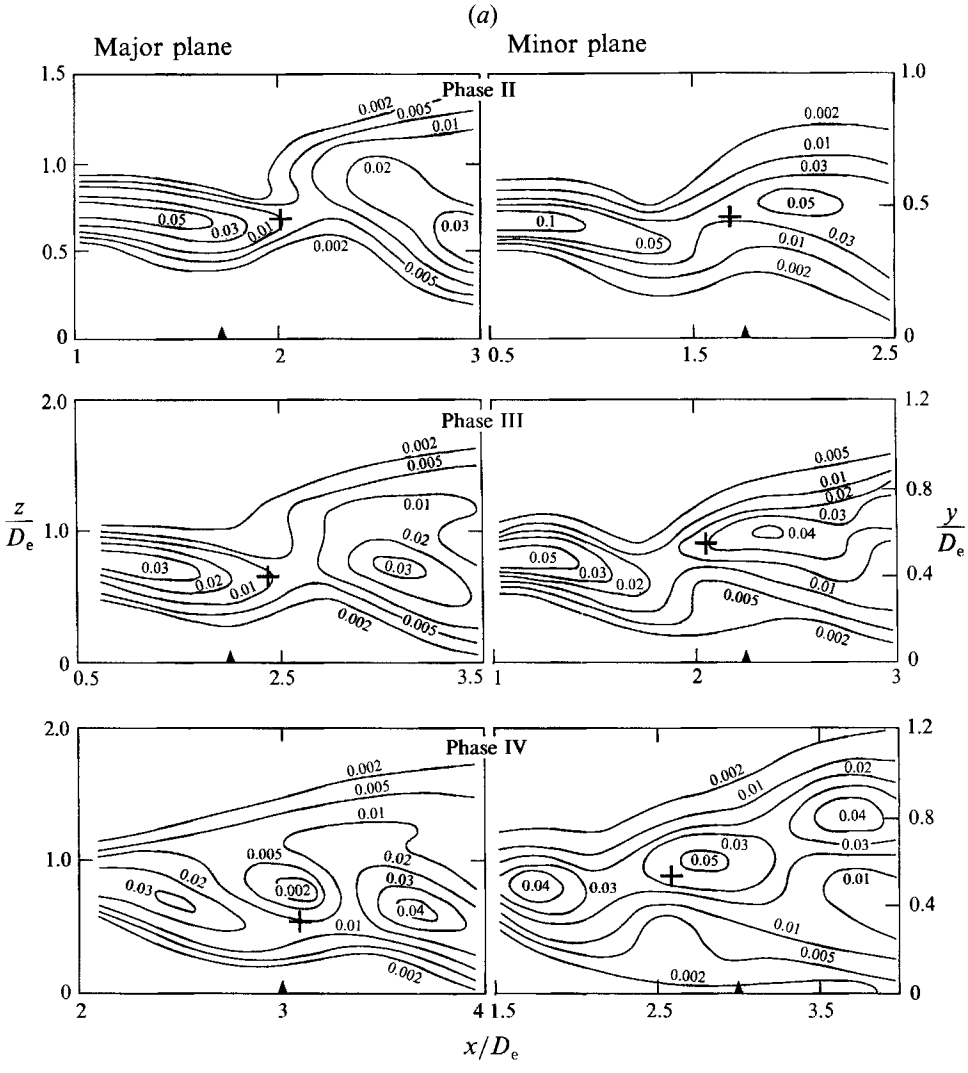

FIGURE 22(a). For caption see page 353.

$-\langle u_r^2\rangle \partial\langle u\rangle/\partial x - \langle v_r^2\rangle \partial\langle v\rangle/\partial y]$. Contours of $\langle P_s\rangle$, $\langle P_n\rangle$ and total production $\langle P\rangle$ [$\equiv \langle P_s\rangle + \langle P_n\rangle$] for the elliptic jet are shown in figure 22(*a–c*), and $\langle P\rangle$ for the circular jet is shown in figure 22(*d*). Coherent strain rate $2\langle S\rangle$ [$\equiv (\partial\langle v\rangle/\partial x + \partial\langle u\rangle/\partial y)$], and normal production terms $\langle P_{nu}\rangle$ and $\langle P_{nv}\rangle$ in the elliptic jet are shown for phase II in figure 23(*a–c*). Since $\langle u_r v_r\rangle$ and $\langle S\rangle$ have similar spatial distributions, namely their peaks occur in the braid, the peak of $\langle P_s\rangle$ necessarily occurs there also. Note that unlike the case of pairing of elliptic structures (Part 2), no negative $\langle P_s\rangle$ is generated during the evolution of the preferred mode structure. Contours of $\langle P_n\rangle$ are quite different from those of $\langle P_s\rangle$, and at each phase, the peak value of $\langle P_s\rangle$ is higher than that of $\langle P_n\rangle$ (by 50–200%). Furthermore, the $\langle P_n\rangle$ distribution contains regions of significant negative values. $\langle P_n\rangle$ values change radially across the roll centre in both planes; while the negative $\langle P_n\rangle$ generally dominates in both planes, the switching of its sign across the centre is quite different in the two planes. After phase III, the negative peaks in $\langle P_n\rangle$ become greater than the positive peaks in both planes; at phase IV, the negative peak in $\langle P_n\rangle$ is about three times greater. Note that

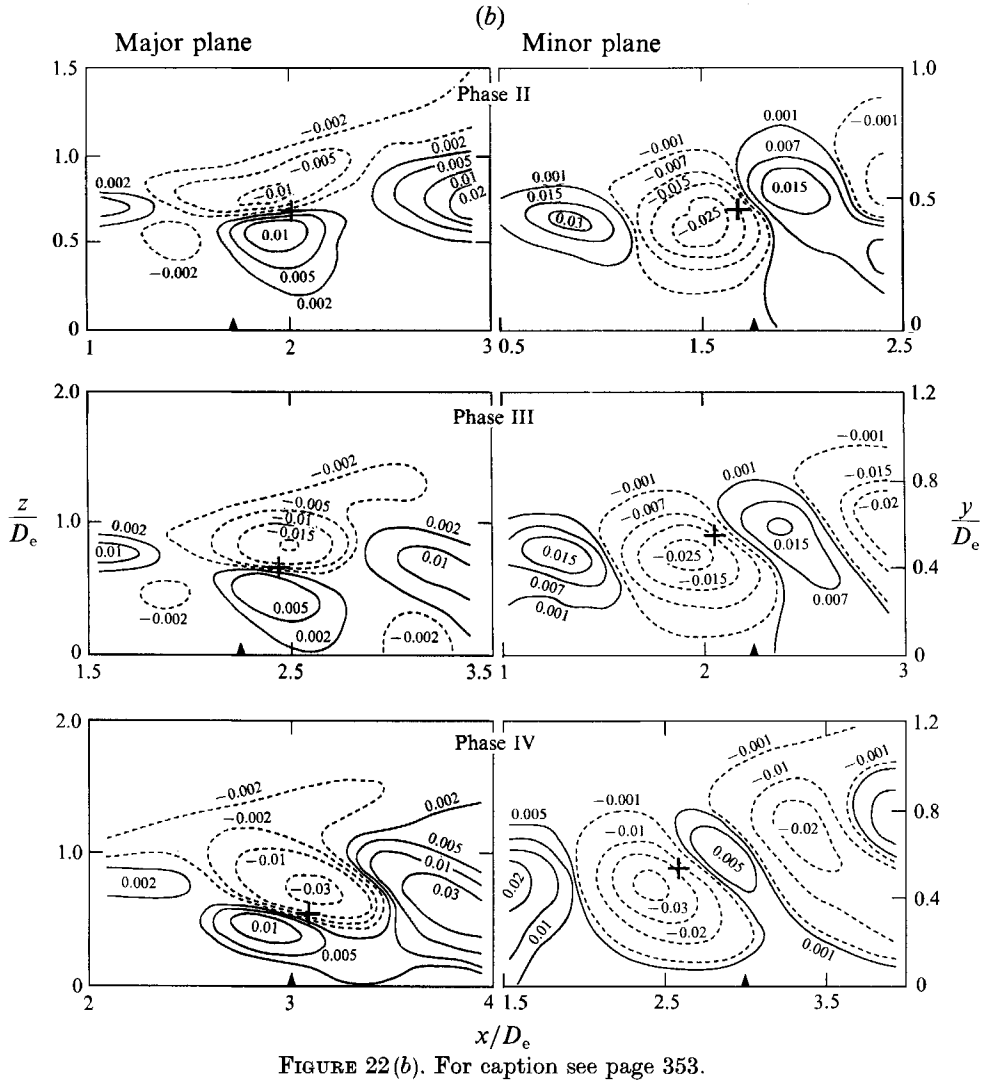

FIGURE 22(*b*). For caption see page 353.

although normal and shear productions are comparable in their peak values, the net contribution of $\langle P_n \rangle$ to an area average is considerably lower because of cancellation of positive- and negative-valued regions. It is interesting to note that in the far fields of jets (Tso 1983), wakes (Hayakawa & Hussain 1985) and mixing layers (Metcalfe *et al.* 1987; Hayakawa & Hussain 1991), $\langle P_n \rangle$ was found to be considerably smaller, and thus $\langle P_s \rangle$ contributed more heavily to $\langle P \rangle$. This apparent disagreement between these studies and the near-field study of elliptic jets has been discussed in Part 2 in terms of the effects of vortical structure curvature.

A comparison of $\langle P \rangle$-contours for elliptic and circular jets shows that the negative production regions are more significant in the elliptic jet than in the circular jet. The $\langle P \rangle$-contours are quite similar in the two planes in phase II, both being similar to $\langle P \rangle$-contours in the circular jet in phase II. At later phases, $\langle P \rangle$-contours are noticeably different between the two planes, and each case is different from $\langle P \rangle$-contours in the circular jet. Note that only incoherent normal stresses contribute to negative $\langle P \rangle$. Peak values of $\langle P \rangle$ in the circular jet are higher than those in the major plane, but are comparable to the peak values in the minor plane of the elliptic

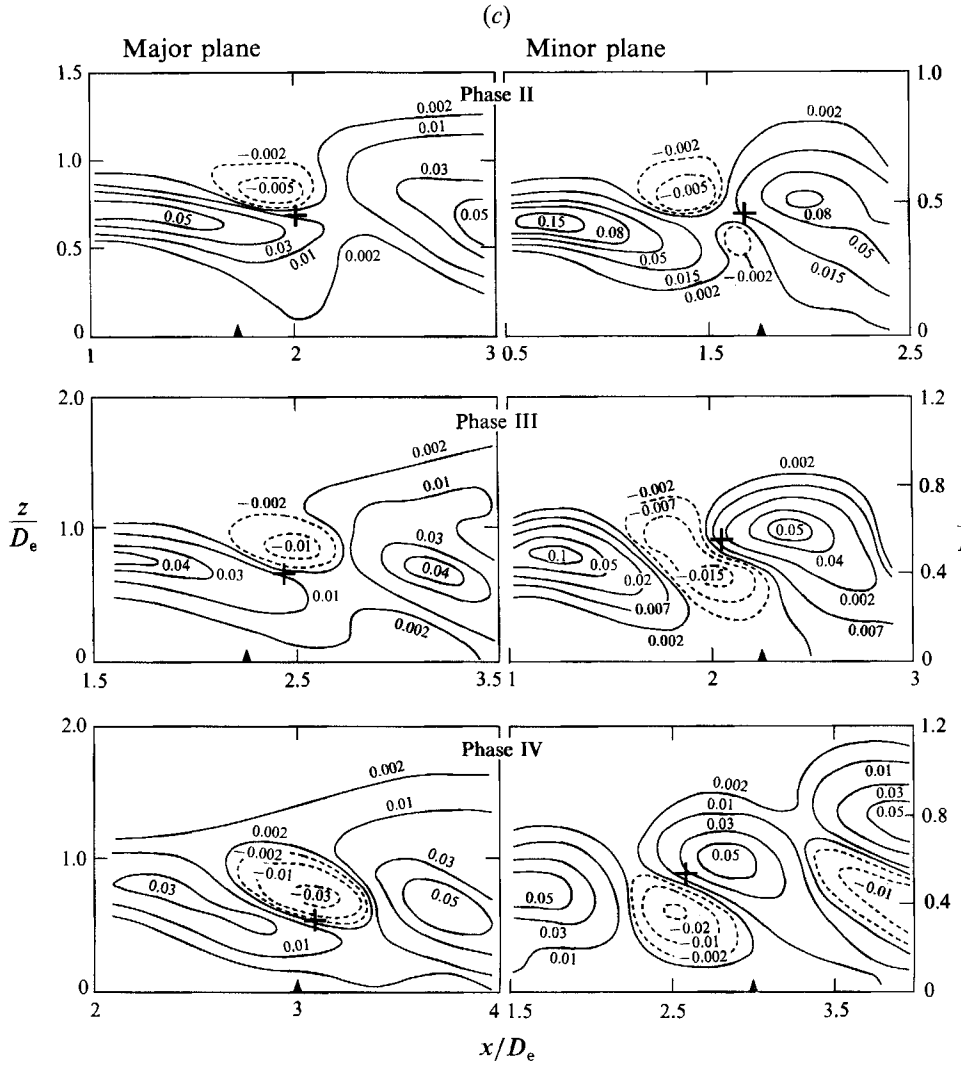

FIGURE 22(c). For caption see facing page.

jet. Distributions of $\langle u \rangle$ at phase I show that the shear layer thickness (defined by the width between the contour levels $\langle u \rangle / U_e = 0.1$ and 0.9) in the major plane increases at a higher rate, and the thickness is almost twice that in the minor plane at $x/D_e = 0.2$. As a result, the peaks in $\langle \omega \rangle$, $\langle S \rangle$, and $\langle P \rangle$ are smaller in the major plane than in the minor plane. However, the area enclosed by a given $\langle P \rangle$-contour (say $\langle P \rangle = 0.002$) is larger in the major plane, implying a higher integrated production in this plane.

The turbulence production mechanism, which involves the stretching of ribs and roll curvature effects, has been discussed in detail in Part 2 for two interacting vortices. In the following, we examine turbulence production for the preferred mode structure evolution in terms of rib stretching in the braid and near the rolls. The shear and normal production terms $\langle P_s \rangle$ and $\langle P_n \rangle$ are dependent on the coordinate system chosen while the total production $\langle P \rangle$ is invariant under rotation of the axes and is therefore a more meaningful quantity. However, a detailed study of the

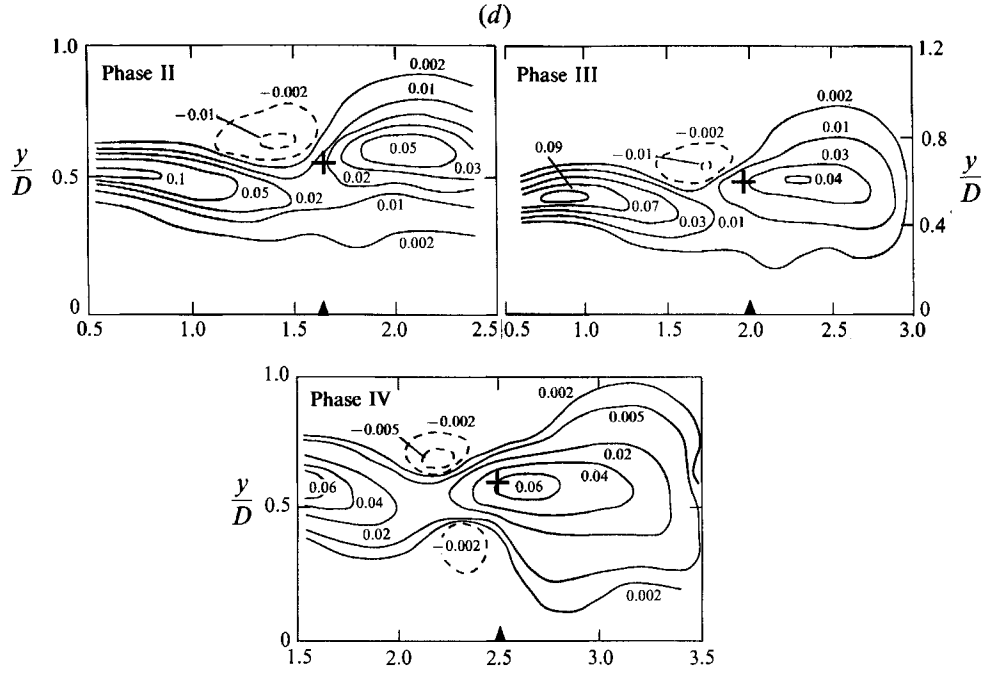

FIGURE 22. Contours of: (*a*) shear production $\langle P_s\rangle/(U_e^2 f)$; (*b*) normal production $\langle P_n\rangle/(U_e^2 f)$; (*c*) total production $\langle P\rangle/(U_e^2 f)$ in the elliptic jet. (*d*) Contours of $\langle P\rangle/(U_e^2 f)$ in the circular jet.

distributions of the terms $\langle P_s\rangle$, $\langle P_{nu}\rangle$ and $\langle P_{nv}\rangle$ in an appropriate coordinate system is very helpful in understanding the physical mechanism of production in turbulent shear flows. A clear understanding of the behaviour of production terms $\langle P_s\rangle$, $\langle P_{nu}\rangle$ and $\langle P_{nv}\rangle$ requires a detailed examination of the strain fields $(\partial\langle u\rangle/\partial y+\partial\langle v\rangle/\partial x)$, $\partial\langle u\rangle/\partial x$ and $\partial\langle v\rangle/\partial y$, and incoherent stresses $\langle u_r v_r\rangle$, $\langle u_r^2\rangle$, and $\langle v_r^2\rangle$. The rolls induce continual stretching of the ribs, resulting in turbulence production. In the usual streamwise, transverse and spanwise (x, y, z) coordinates, $\langle P_s\rangle$ is the greatest contributor to the total turbulence production in the braid due to rib stretching induced by corotating neighbouring rolls. The $\langle P_s\rangle$ distribution confirms that most of the turbulence produced by $\langle u_r v_r\rangle$ occurs in the braid.

The effect of azimuthal roll curvature on the strain rates $\partial\langle u\rangle/\partial x$ and $\partial\langle v\rangle/\partial y$ has been discussed in Part 2. Contours of $-\partial\langle u\rangle/\partial x$, $\langle u_r^2\rangle$, $\langle P_{nu}\rangle$ $[=-\langle u_r^2\rangle\partial\langle u\rangle/\partial x]$, $-\partial\langle v\rangle/\partial y$, $\langle v_r^2\rangle$ and $\langle P_{nv}\rangle[=-\langle v_r^2\rangle\partial\langle v\rangle/\partial y]$ are shown schematically in figure 24(*a–f*) respectively. Note that curvature has very little effect on the gradient $\partial\langle v\rangle/\partial y$, but its effect on $\partial\langle u\rangle/\partial x$ is quite significant; as a result, $\langle P_{nv}\rangle$ shows a four-lobed distribution with positive and negative regions occurring alternately, while $\langle P_{nu}\rangle$-contours show two dominant regions. The measured contours of $\langle P_{nu}\rangle$ and $\langle P_{nv}\rangle$ shown in figure 23(*b, c*) are similar to the schematic distributions shown in figure 24(*c, f*).

Considering such strain fields and the regions of rib and roll interaction, regions of high $\langle P_{nu}\rangle$ and $\langle P_{nv}\rangle$ are shown schematically in figure 24(*g, h*). In figure 24(*g*), the ribs in the interacting regions labelled A1 and A2 are stretched in the y-direction, producing positive $\langle P_{nu}\rangle$, while their compression in the y-direction at N1 and N2 produces negative $\langle P_{nu}\rangle$. In the regions labelled A3 and A4 (figure 24*h*), the ribs are stretched in the x-direction, resulting in positive $\langle P_{nv}\rangle$; rib compression at N3 and

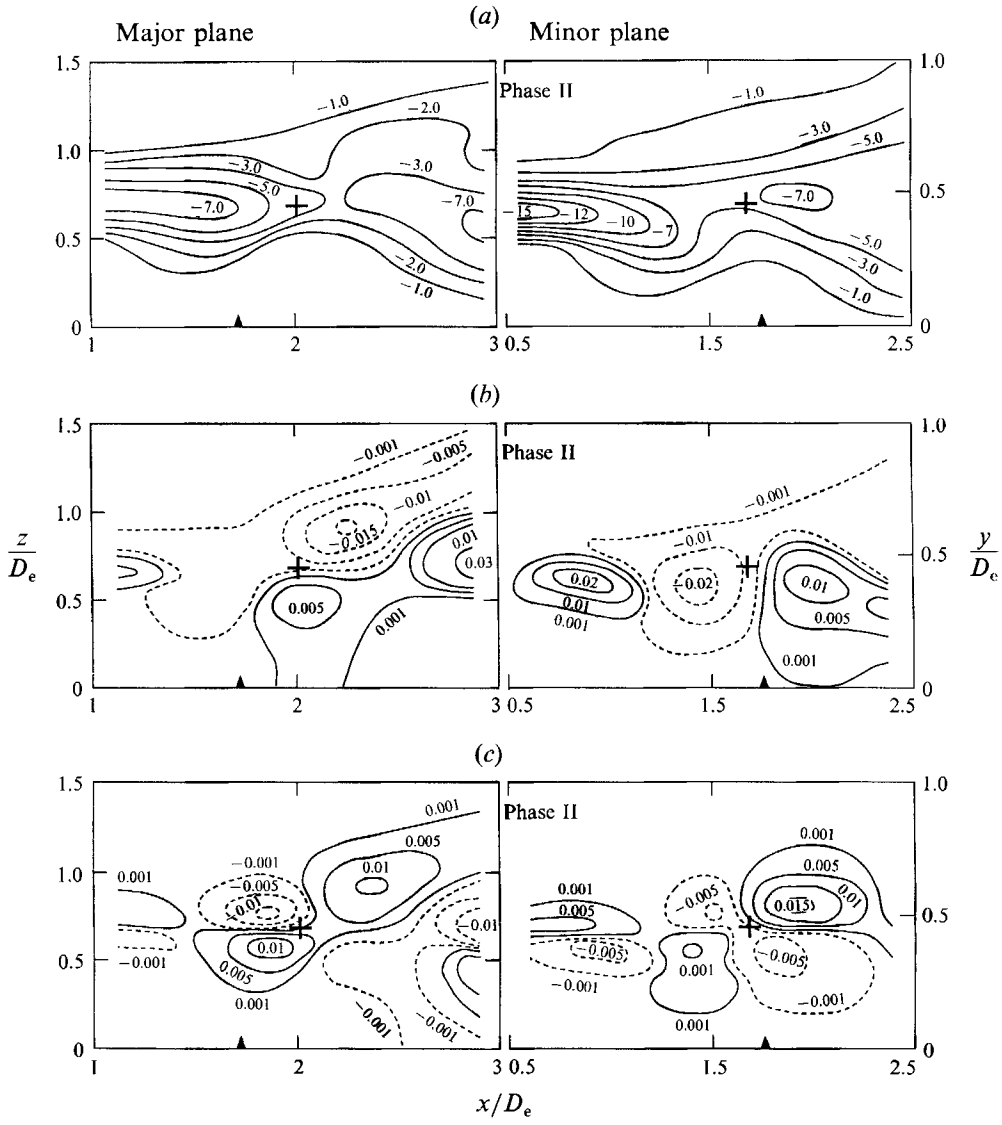

FIGURE 23. Contours of: (*a*) strain rate $2\langle S\rangle/f$; (*b*) $\langle P_{nu}\rangle/(U_e^2 f)$; (c) $\langle P_{nv}\rangle/(U_e^2 f)$ at phase II.

N4 produces negative $\langle P_{nv}\rangle$. This simplified picture of $\langle P_{nu}\rangle$ and $\langle P_{nv}\rangle$ distributions is fairly consistent with the experimental measurements (see figure 23*b*, *c*).

3.4. *Time-average characteristics*

The motivation for this section is to investigate how the time-average measures are modified by excitation at the preferred mode frequency and to examine these data in the context of the coherent structures present. Corresponding data for coherent structure pairing were discussed in Part 2. The data presented in this paper and their comparison with time-average data in Part 2 should re-emphasize the point that time-average data do retain some influence, thus information, about the coherent structures. Furthermore, these measures may serve as a database for validation of turbulence models and direct numerical simulations.

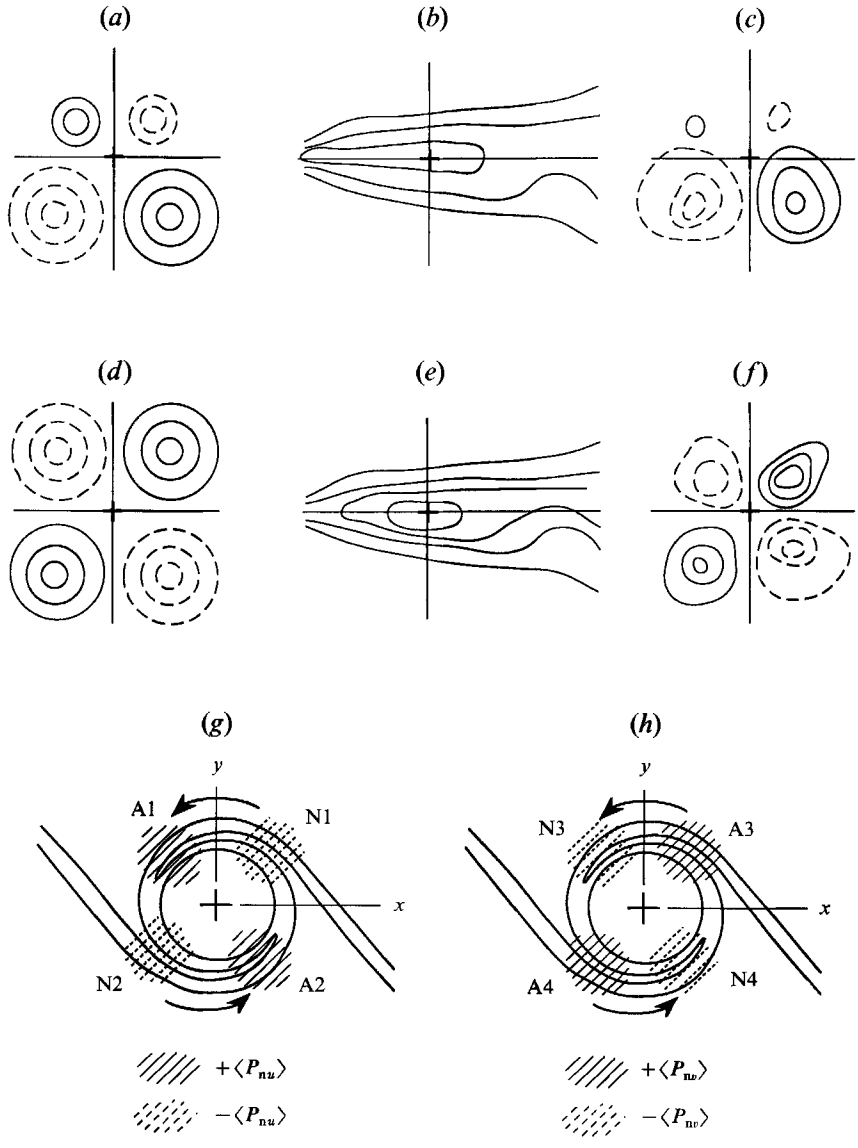

FIGURE 24. Qualitative contours of: (*a*) $-\partial\langle u\rangle/\partial\langle x\rangle$; (*b*) $\langle u_r^2\rangle$; (*c*) $\langle P_{nu}\rangle = -\langle u_r^2\rangle\partial\langle u\rangle/\partial\langle x\rangle$; (*d*) $-\partial\langle v\rangle/\partial\langle y\rangle$; (*e*) $\langle v_r^2\rangle$; (*f*) $\langle P_{nv}\rangle = -\langle v_r^2\rangle\partial\langle v\rangle/\partial\langle y\rangle$; (*g*, *h*) Schematics showing the regions of positive and negative $\langle P_{nu}\rangle$ and $\langle P_{nv}\rangle$ of the preferred mode structure due to rib–roll interaction.

3.4.1. *Longitudinal and transverse velocities*

The contours of longitudinal mean velocity U, non-dimensionalized by both the local centreline mean velocity U_c and exit velocity U_e are shown in figure 25(*a*, *b*), respectively. The contours of U/U_c show that excitation pushes the entire shear layer outward (within the measurement region) in both planes. This effect of excitation is more pronounced in the major plane, where the outer boundary (i.e. $U/U_c = 0.1$) is pushed outward considerably, while the inner boundary (i.e. $U/U_c = 0.9$) is pushed toward the jet axis for $x/D_e < 10$. The increase in the shear layer thickness is about 100% in the major plane and about 50% in the minor plane at $x/D_e = 5$. In the

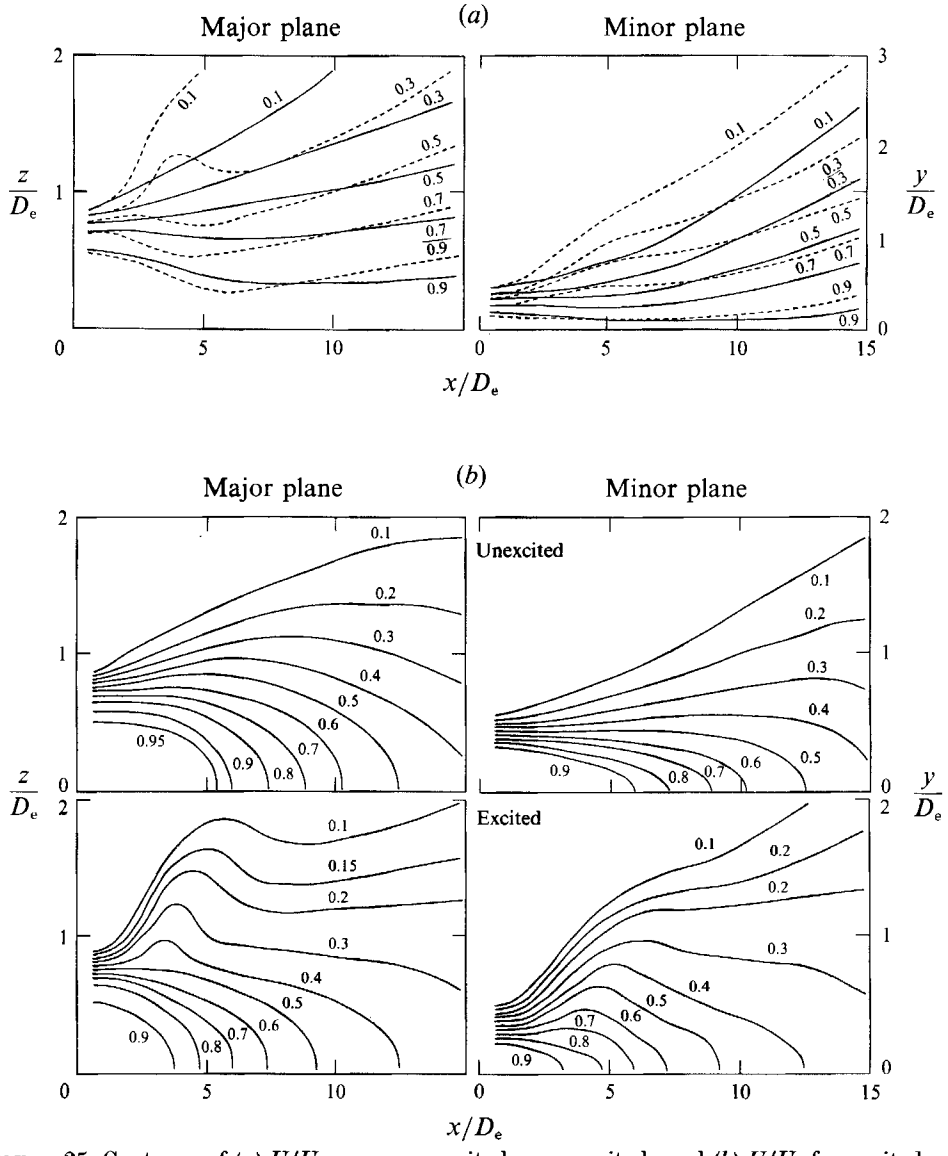

FIGURE 25. Contours of (*a*) U/U_c: ——, unexcited; ----, excited; and (*b*) U/U_e for excited and unexcited elliptic jets.

major plane up to $x \approx 5$, the inward and outward inclinations of the $U/U_c \geqslant 0.5$ and $U/U_c < 0.5$ contours are consistent with the fact that the vortex core moves toward the jet axis, leaving behind low-vorticity fluid which diffuses outward (figure 4). Because of an early switching of axes of the excited preferred mode structures (for details, see Part 1), the contours of U/U_c for $x > 5$ show an increase in inclination (from negative to positive) in the major plane, but an inclination decrease in the minor plane.

Since the centreline velocity U_c decreases downstream of the potential core's end, U/U_c does not show the effect of excitation on the potential core length. This is more clearly apparent in the U/U_e contours (figure 25*b*). Note that the location where the $U/U_e = 0.9$ line intersects the jet axis has moved from $x/D_e \approx 6$ to 4. Excitation at

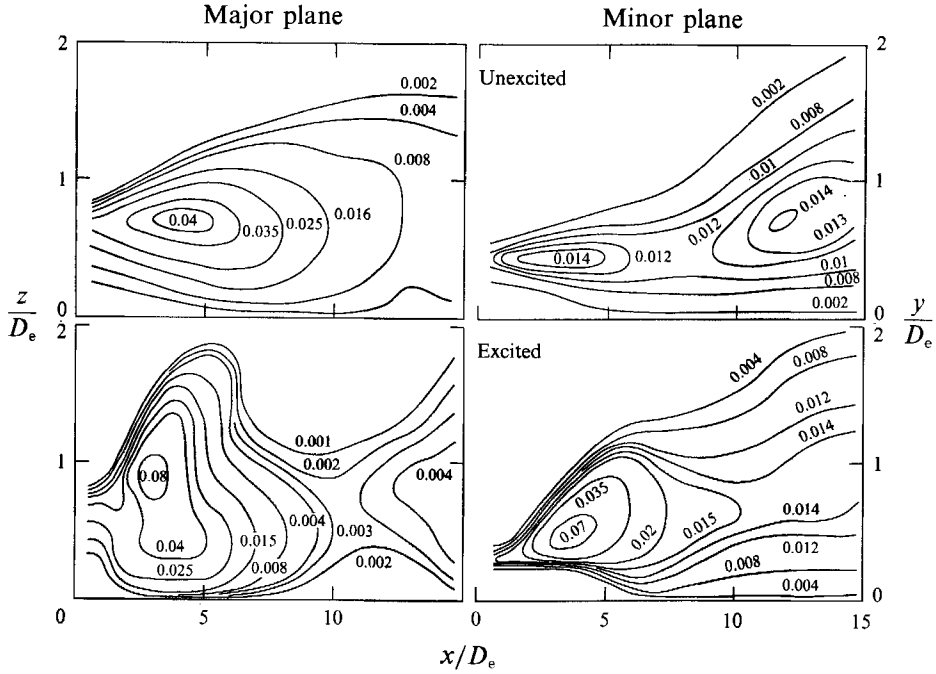

FIGURE 26. V/U_e contours for excited and unexcited elliptic jets.

the preferred mode frequency therefore shortens the potential core, but the effect is not as dramatic as for excitation at the jet column pairing mode (Part 2).

The U/U_e contours show that the initial linear spread of the shear layer in the unexcited case is noticeably altered by the excitation. The slope of a constant U/U_e line, say $U/U_e = 0.2$, increases initially, attains a constant value and then decreases. In fact, this slope becomes negative in the major plane. Owing to excitation, spatially localized events, namely structure formation, growth, and switching of axes, leave strong 'footprints' on the time-average measures, causing significant changes in the slope of U/U_e.

Excitation produces a more profound effect on time average V than U. Contours of V/U_e (figure 26) also exhibit significant widening due to excitation. Excitation increases the peak values of V/U_e by about 100% in the major and 400% in the minor plane. Spatial jitter in the formation of structures in the unexcited jet produces lower peak values of V/U_e than in the excited case. The effects of rotational and self-induced motions of elliptic vortical structures on the transverse velocity field have been discussed in Part 2. Both unexcited and excited jets show no (time-average) negative V/U values, although individual structures are associated with positive and negative transverse velocities (figure 16*a*). Because the positive (outward) transverse velocity in front of the rolls is higher than the negative (inward) velocity on their upstream side, the time-average V-contours show only positive values.

3.4.2. *Turbulence intensities and Reynolds stress*

In contrast to phase-average r.m.s. intensities $\langle u_r^2 \rangle^{\frac{1}{2}}$ and $\langle v_r^2 \rangle^{\frac{1}{2}}$, we denote their time-average r.m.s. values by u' and v'. Contours of u'/U_e (figure 27) show two peaks under excitation in both the major and minor planes, while only one peak occurs in the unexcited state. In the excited case, the first peak is due to the spatially localized

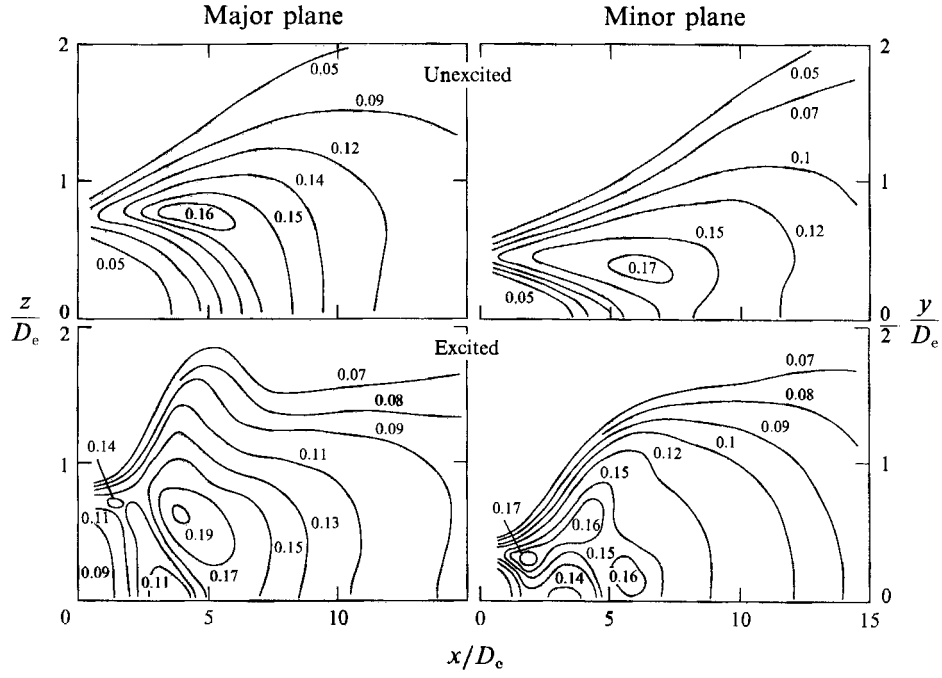

FIGURE 27. u'/U_e contours for excited and unexcited elliptic jets.

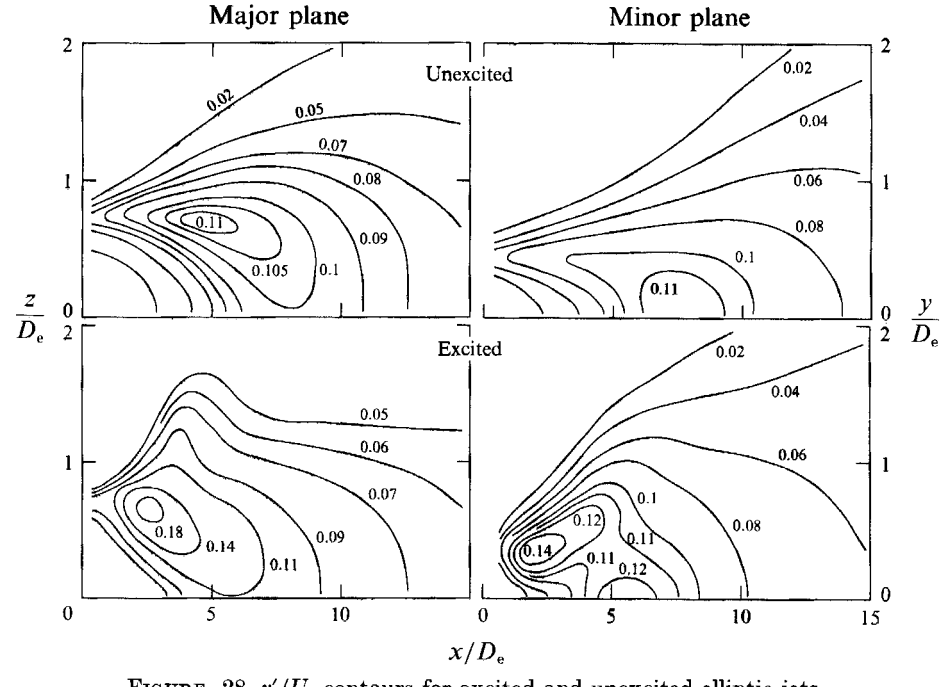

FIGURE 28. v'/U_e contours for excited and unexcited elliptic jets.

rollup of the preferred-mode structures, while the second peak is attributed to the breakdown of the structure. In the unexcited case, weaker structures with spatial jitter form and break down thereafter. As a result, time-average u'/U_e contours do not show clear and separate peaks. Instead, a broad peak in u'/U_e contours is visible.

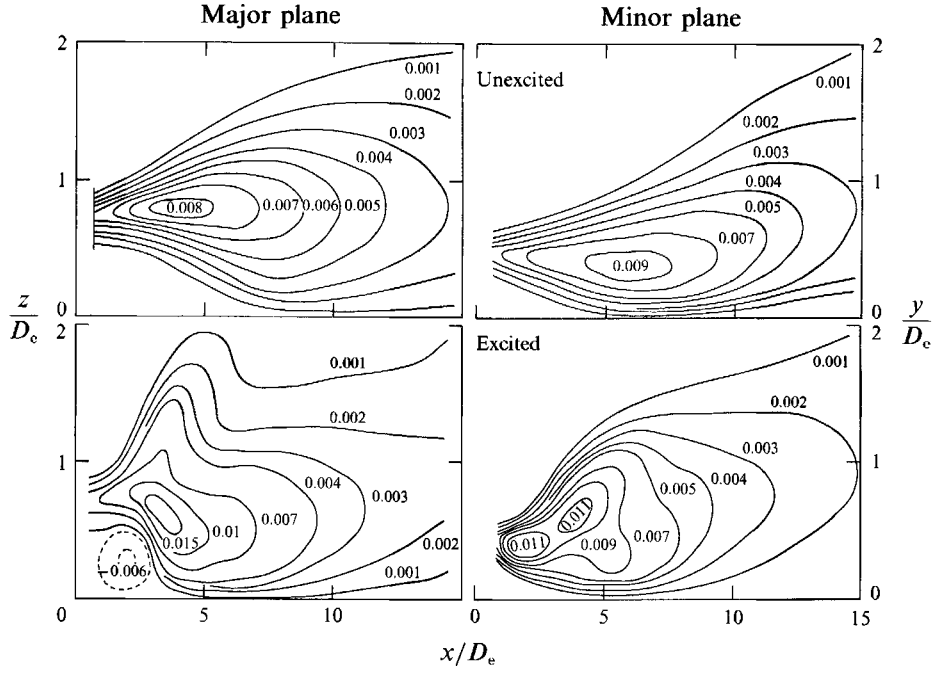

FIGURE 29. $\overline{uv}/U_e^2$ contours for excited and unexcited elliptic jets.

Contours of v'/U_e (figure 28) show a single peak slightly downstream of the corresponding u'/U_e peak in both planes. Under excitation, the contours exhibit greater spread, and the peak location moves upstream due to earlier preferred mode rollup.

Time-averaged Reynolds stress contours $\overline{uv}/U_e^2$ are shown in figure 29. A small region of negative $\overline{uv}/U_e^2$ is observed only in the major plane for the excited case. This is the 'footprint' of comparatively large negative coherent Reynolds stress (figure 21). In the major plane, excitation produces a significant amount of counter-gradient momentum transport which is detectable even in the time-averaged domain. Excitation increases the peak value of $\overline{uv}/U_e^2$ by about 90% in the major plane and 20% in the minor plane.

4. Concluding remarks

Because of experimental limitations, we have studied various coherent structure properties of an elliptic jet in its two symmetry planes only, namely the major and minor planes. Conceptually, through a sophisticated conditional sampling technique using a rake of X-wires (Hayakawa & Hussain 1985; Antonia & Britz 1989) it is possible to study three-dimensional structures including ribs. However, the probe size and probe interference limit the effectiveness of a multi-rake hot-wire measurement technique, particularly in the thin near-exit jet shear layer region. Instead, we have strived to infer and discuss the three-dimensional dynamics of coherent structures from these limited, yet detailed, data. Numerical experiments and future three-dimensional measurement techniques (such as holographic particle displacement velocimetry) are also viable candidates for such studies. We have used direct numerical simulation to study the three-dimensional evolution of the preferred mode structure and the generation of streamwise vortices (ribs) in a temporally

evolving elliptic jet. Such a collaboration between laboratory experiments and numerical simulations allowed us to achieve an understanding of the three-dimensional dynamics of the elliptic-jet preferred mode structure, including the mechanism of rib formation, turbulence production, and entrainment and mixing.

A mechanism for rib formation is proposed based on the influence of mutual- and self-induction of the rolls on vortex lines in the braid. We then corroborate our proposed rib generation mechanism using simulation data. Numerical results revealed that, unlike in an axisymmetric jet, stronger ribs form in the braid and join the neighbouring rolls at preferred locations. Such spatially localized rib–roll interaction produces higher entrainment and mixing in an elliptic jet than in an axisymmetric jet. Computed entrainment data from the phase-averaged velocities reveal that indeed the entrained mass in the elliptic-jet preferred mode structure is higher than that in a circular jet.

In the present method of phase-locked measurement, the question arises as to how much the spatial jitter of the structures influences measurement of vorticity and other associated dynamical quantities. Since low-level excitation at the preferred mode frequency organizes the most probable structure and generates structures of similar size, shape and strength, and because the eduction of the structure at a particular location is triggered by the local structure's footprint itself, the educed coherent structure characteristics are not subject to significant smearing due to phase jitter.

The authors are grateful to Dr Mogens V. Melander for fruitful discussions and for providing the numerical simulation code, to Dr Amit Basu and Mr Ernest F. Hasselbrink for providing the numerical results, and to Mr Wade Schoppa for careful review of the manuscript. The work was supported by the Office of Naval Research Grant N00014-89-J-3231.

REFERENCES

Antonia, R. A. & Britz, D. 1989 *Exps. Fluids* **7**, 138.

Arms, R. J. & Hama, F. R. 1965 *Phys. Fluids* **8**, 553.

Batchelor, G. K. 1967 *An Introduction to Fluid Dynamics*. Cambridge University Press.

Bridges, J. E. & Hussain, F. 1988 Evolution of noncircular vortex rings. In *Proc. 12th World Congr. on Scientific Computation, Paris, July 18–22.*

Cantwell, B. & Coles, D. 1983 *J. Fluid Mech.* **136**, 321.

Coles, D. E. 1962 *Rand Corp. Rep.* R-403-PR.

Corcos, G. M. & Sherman, F. S. 1984 *J. Fluid Mech.* **139**, 29.

Crow, S. C. & Champagne, F. H. 1971 *J. Fluid Mech.* **48**, 547.

Gutmark, E. & Ho, C. M. 1983 *Phys. Fluids* **26**, 2932.

Hayakawa, M. & Hussain, A. K. M. F. 1985 In *5th Symp. on Turbulent Shear Flows*, p. 4.33. Cornell University.

Hayakawa, M. & Hussain, F. 1993 Turbulence structure of a self-preserving plane mixing layer. (submitted).

Ho., C. M. & Gutmark, E. 1987 *J. Fluid Mech.* **179**, 383.

Husain, H. S. 1984 An experimental investigation of unexcited and excited elliptic jets. Ph.D. thesis, University of Houston.

Husain, H. S. & Hussain, A. K. M. F. 1983 *Phys. Fluids.* **26**, 2763.

Husain, H. S. & Hussain, F. 1991 *J. Fluid Mech.* **233**, 439.

Hussain, A. K. M. F. 1983 *Phys. Fluids* **26**, 2816.

Hussain, A. K. M. F. & Clark, A. R. 1981 *J. Fluid Mech.* **104**, 263.

HUSSAIN, A. K. M. F. & ZAMAN, K. B. M. Q. 1980 *J. Fluid Mech.* **101**, 493.

HUSSAIN, A. K. M. F. & ZAMAN, K. B. M. Q. 1981 *J. Fluid Mech.* **110**, 39.

HUSSAIN, F. & HUSAIN, H. S. 1989 *J. Fluid Mech.* **208**, 257.

LASHERAS, J. C., CHO, J. S. & MAXWORTHY, T. 1986 *J. Fluid Mech.* **172**, 231.

LASHERAS, J. C. & CHOI, H. 1988 *J. Fluid Mech.* **189**, 52.

LEE, C., METCALFE, R. W. & HUSSAIN, F. 1991 *Turbulent Shear Flows* **7**, pp. 331–343. Springer.

MARTIN, J. E. & MEIBURG, E. 1991 *J. Fluid Mech.* **230**, 271.

MEIBURG, E. & LASHERAS, J. C. 1988 *J. Fluid Mech.* **190**, 1.

MELANDER, M. V. & HUSSAIN, F. 1992 New perspectives on vorticity dynamics (submitted).

MELANDER, M. V., HUSSAIN, F. & BASU, A. 1991 Breakdown of a circular jet into turbulence. In *8th Symp. on Turb. Shear Flow, Munich, Sept. 9–11.*

METCALFE, R., HUSSAIN, F., MENON, S. & HAYAKAWA, M. 1987 In *Turbulent shear flows 5* (ed. F. Durst *et al.*), p. 110. Springer.

PIERRHUMBERT, R. T. & WIDNALL, S. E. 1982 *J. Fluid Mech.* **114**, 59.

RICOU, F. P. & SPALDING, D. B. 1961 *J. Fluid Mech.* **11**, 21.

ROGERS, M. M. & MOSER, R. D. 1992 *J. Fluid Mech.* **243**, 183.

TSO, J. 1983 Coherent structures in a fully-developed axisymmetric jet. Ph.D. thesis, The Johns Hopkins University.

TSO, J. & HUSSAIN, F. 1989 *J. Fluid Mech.* **203**, 225.

TSUCHIYA, Y., HORIKOSHI, C. & SATO, T. 1984 On the spread of rectangular jets. In *Turbulence Symp.* p. 15.1 (U. of Missouri-Rolla).

ZAMAN, K. B. M. Q. & HUSSAIN, A. K. M. F. 1980 *J. Fluid Mech.* **101**, 449.